Diploma Thesis

Ray Tracing and Measurement based Evaluation of RFID Localization Methods

performed at the

Institute of Electrodynamics, Microwave and Circuit Engineering
Technische Universität Wien

supervised by

Assoc. Prof. Dipl.-Ing. Dr. techn. Holger Arthaber
and
Univ. Ass. Dipl.-Ing. Bernhard Pichler, BSc.

by

Stefan Hechenberger, BSc.
Matr. Nr. 01528155

Vienna, July 14, 2019

Abstract

The localization of radio frequency identification (RFID) tags opens the door to countless applications in the field of object tracking. Harvesting their operating power from the continuous wave signal transmitted by the RFID reader, passive tags forego the use of batteries. This property renders their utilization very beneficial in many applications. The present thesis deals with a passive RFID system, operating in two frequency regimes, at 860–960 MHz and at 2.45 GHz.

A novel method, that superimposes a low power wideband signal onto the continuous wave signal, enables accurate time of flight range estimation within off-the-shelf RFID systems. The focus of this thesis is to evaluate state of the art localization techniques based on this method. To this end, a three dimensional wideband ray tracer is implemented in order to simulate the backscatter channel of an indoor RFID system. In addition, the results of a comprehensive measurement campaign are used. The range estimation is performed by a simple matched filter approach and a more sophisticated maximum likelihood estimator. A comparison of the ranging based on the synthetic and the measured data allows for a statement about the limitations of a practical RFID system.

It is shown, that the simulated channel model provides a good approximation of the true channel. Further, it is observed, that a location specific channel estimation and knowledge about the tags' impulse response are crucial for the accuracy of the range estimation.

Kurzfassung

Die Lokalisierung von Radio Frequency Identification (RFID) Tags öffnet die Tür zu unzähligen Anwendungen im Gebiet der Objektverfolgung. Indem passive Tags ihre Versorgungsleistung dem Trägersignal des RFID Readers entnehmen, verzichten sie auf den Gebrauch von Batterien. Damit erweist sich ihr Einsatz in vielen Anwendungsfällen als vorteilhaft. Die vorliegende Arbeit beschäftigt sich mit einem passiven RFID-System, das in zwei Frequenzbereichen, bei 860–960 MHz und bei 2.45 GHz, arbeitet.

Eine neue Methode überlagert dem kontinuierlichen Trägersignal ein leistungsschwaches Breitbandsignal, um eine Time-of-Flight-basierte Abstandsschätzung in handelsüblichen RFID-Systemen zu ermöglichen. Der Fokus dieser Arbeit liegt in der Bewertung moderner Lokalisierungsverfahren, basierend auf dieser Methode. Zu diesem Zweck wird ein dreidimensionaler Raytracer implementiert, um den Backscatterkanal eines RFID-Systems zu simulieren. Zusätzlich werden die Resultate einer umfassenden Messkampagne ausgewertet. Die Abstandsschätzung erfolgt mittels einem einfachen Korrelationsfilter und einem erweiterten Maximum-Likelihood-Schätzer. Durch einen Vergleich der Lokalisierungsmethoden, basierend auf den synthetischen und den gemessenen Daten, kann eine Aussage über die Limitierungen eines praktischen RFID-Systems getroffen werden.

Es wird gezeigt, dass das simulierte Modell eine gute Näherung des tatsächlichen Kanals darstellt. Weiters wird offengelegt, dass die positionsspezifische Kanalschätzung und die Berücksichtigung der Impulsantwort des Tags entscheidend für die Genauigkeit der Abstandsschätzung sind.

Acknowledgements

I would like to thank all members of the Microwave Engineering Group at TU Wien. My special thanks go to Dipl.-Ing. Daniel Neunteufel and Dipl.-Ing. Florian Galler, who always supported me with their profound knowledge.
Further, I want to thank my supervisors Assoc. Prof. Dipl.-Ing. Dr. techn. Holger Arthaber and Univ. Ass. Dipl.-Ing. Bernhard Pichler for their detailed review of this thesis.

This thesis was supported by the Christian Doppler Laboratory for Location-aware Electronic Systems.

Table of Contents

List of Figures

Abbreviations

AoA angle of arrival

AoD angle of departure

AWGN additive white Gaussian noise

cdf cumulative distribution function

CW continuous wave

DSSS direct sequence spread spectrum

EPC electronic product code

HF high frequency

IC integrated circuit

ISM industrial, scientific, and medical

KL divergence Kullback-Leibler divergence

LF low frequency

LO local oscillator

LOS line of sight

MAP maximum a posteriori

MF matched filter

MIMO multiple input multiple output

ML maximum likelihood

MPC multipath component

pdf probability density function

PDP power delay profile

RCS radar cross section

RFID radio frequency identification

RSS received signal strength

SDR software defined ratio

SNR signal-to-noise ratio

TDL tapped delay line

TE transversal electric

TM transversal magnetic

ToF time of flight

TSS transmit signal strength

UHF ultra high frequency

1 Introduction

Radio frequency identification (RFID) is a technology to identify and track physical objects based on the transmission of electro-magnetic waves. Supply-chain management, building access control, traffic control and advertising are only a few examples from the vast variety of applications in which RFID is used [1, 2, 3]. In many areas of automatic identification, barcode has been the pervasive technology for decades. However, technical possibilities provided by the optical recognition of a binary code through a laser are restricted by various factors. Primarily, there has to be an unobstructed line of sight between the barcode and the laser. Objects, dirt, or liquids easily violate this requirement. Another limiting aspect is the lacking opportunity of storing data in addition to an identification number [3, 4]. The ability to overcome these boundaries and the lowering prices of its components nominate RFID as a promising candidate in many applications that involve object identification.

An RFID system is composed of two main elements: A uniquely identifiable tag (or label), consisting of a small integrated circuit (IC) attached to an antenna, and a reader (or interrogator) that reads data from or writes data to the tag. Various systems may be categorized by their transmission frequency, the tags power supply or the transmission range. This work deals with a far field system operating in the ultra high frequency (UHF) regime at 860–960 MHz and in the industrial, scientific, and medical (ISM) band at 2.45 GHz. The tags are passive, which means they are not connected to a power supply, but harvest their operating power from the radio energy transmitted by the reader. Data transmission from the tag to the reader is possible by the use of passive backscattering, first introduced by Stockman in 1948 [5]. The missing need for a battery at the tag brings two major advantages with it: (i) Tags can be made extremely thin, such that they barely differ from a barcode sticker in size. (ii) Replacing empty batteries for a large number of tags is impractical or even infeasible, which is avoided by passive tags.

Dealing with object identification, the thought of possibilities to determine the objects' precise position is natural. RFID's system architecture, with the reader acting as transmitter/receiver (transceiver) and the tag as reflector, strongly suggests the use of radar techniques. One physical relation that radar makes use of is between the velocity of an electro-magnetic signal and the traveled distance per time period. While the velocity is the known parameter, the time period of a signal traveling from the reader to the tag and back is measured. Consequently, the distance between reader and tag can be estimated. It is an obvious, yet fundamental observation, that the accuracy of such a parameter estimation is

limited by the physical system and the environment it is used in. Within these boundaries it is the task of clever engineering to get as close as possible to the true value. Extensive effort has been made in the research of radar signals [6] and the signal processing within radar systems [7].

A novel method, developed in [8], places the radar functionality on top of an existing standard RFID system by means of a superimposed wideband signal. The present thesis addresses the evaluation of localization algorithms based on this method. In order to assess the behavior of those algorithms with respect to a practical RFID system, a measurement setup is emulated by a computer simulation and the results of both approaches are compared.

Chapter 2 gives an introduction into three elementary subjects with respect to this work: RFID, radar, and parameter estimation. The discussion is thereby restricted to aspects that are most important for the remainder of this text. Chapter 3 provides a probabilistic parameter estimation approach for the localization of RFID tags. For two different channel models, this leads to a simple matched filter estimator and a more elaborate, iterative maximum likelihood estimator. In Chapter 4, the simulation of RFID backscatter channels, and in Chapter 5, the measurement setup, used for the evaluation of the provided algorithms, are described. The results are discussed in Chapter 6, and Chapter 7 gives a conclusion on the presented work.

2 RFID, Radar, and Parameter Estimation

This chapter is intended to provide an individual discussion on the three topics that build the foundation for this work. A rather informal treatment of RFID basics is given in Section 2.1. Section 2.2 considers the most important radar techniques with respect to this work. Section 2.3 starts with a general discussion of optimum parameter estimation and closes the chapter with a contemplation of two approximate estimation schemes.

2.1 RFID Fundamentals

The term "RFID" rather describes a system architecture than a specific implementation. Every RFID system consists of a reader and a tag[1]. A reader is an RF transmitter/receiver (transceiver) combined with a signal processing unit, connected to an antenna. The tags considered in this text consist of a small IC connected to an antenna. They are capable of a few rudimentary operations and comprise a very small data storage. In general, RFID systems can be classified mainly by the following two properties:

Operating Frequency

The most common frequency bands used by RFID systems are the low frequency (LF) band at 125 kHz, the high frequency (HF) band at 13.56 MHz, the UHF band at 860–960 MHz, and the ISM band at 2.45 GHz [3]. Coupled to the operating frequency is the transmission range. Systems in the LF and HF range use *inductive coupling* between the reader and tag antenna for communication, i.e., they operate in the near field of the transmit antenna. Application examples are cashless payment systems or building access control. Systems in the UHF regime and above use *radiative coupling* between the reader and the tag antenna, i.e., they operate in the far field. Presumably the most important application area at this point is object tracking within the supply chain.

[1] A practical RFID system usually has to deal with a large number of tags, which is implied by the task of object identification. In the following work, an existing implementation of multiple access schemes is assumed and therefore, only one tag is considered in the environment.

Power Supply

Another distinction of RFID systems is based on the power supply of the tags. In *active* systems, the tags have their own power supply, for example a battery. This enables tags to transmit information without any preceding action of the reader, and the transmission range is usually higher than for tags without power supply. However, batteries have to be changed or recharged from time to time, which poses a problem for a large number of tags. Furthermore, the tags themselves are extremely thin, which is important for many use cases. This property is lost with an additional battery.
In contrast, tags in a *passive* system do not have their own power supply. They harvest all the energy they need for operation from the RF carrier transmitted by reader. As this is a solution to the problems stated for active systems, passive systems are very interesting for many applications. Nevertheless, the communication range and the computational power are much less than for active tags.

This work deals with a passive UHF RFID system at 860–960 MHz and 2.45 GHz based on the widely deployed EPC Class-1 Gen-2 UHF RFID standard [9], which follows an interrogator-talks-first concept. It specifies that a tag only responds to a query transmitted by the reader. For the communication with passive tags the reader continues transmitting an unmodulated RF carrier after the query. The tag answers by modulating the impedance connected to the antenna, thereby varying the amplitude of the signal reflected back to the reader. This way of data transmission is also referred to as passive backscattering.
The EPC standard defines many specifications that reach from the physical air interface to the communication protocol, e.g., the modulation formats used by the reader and tag, the use of multiple access schemes, or spectral limitations. In addition to the requirements a system has to meet for standard compliance, it may implement optional operations, as long as they do not contradict with the standard regulations. This possibility is exploited in [8], where a ranging method is placed on top of an existing EPC compliant RFID system. As the present work builds on this method, it is described in detail in Section 3.1.

2.2 Radar Principles

Radar, originally from *ra*dio *d*etection *a*nd *r*anging, is a system to determine the range, velocity, or angle of an object. A basic radar system is composed of a radio transceiver, one or more antennas, and a signal processing unit. The radar signal transmitted by the antenna reflects off an object and is received by either the same antenna in a monostatic setup, or by a separate antenna in a bistatic setup. The physical relation between the observation and the parameter of interest determines the required investigation of the received signal. Consequently, the design of the system and the choice of the transmit signal are dependent on the specific application and the parameters to be estimated. To elaborate this in a formal way, three important radar models are described.

Amplitude Model

The power P_i captured by a point receiver at a distance d from an isotropically radiating transmitter with transmit power P_t is

$$P_i = \frac{P_t}{4\pi d^2} \,. \tag{2.1}$$

If an object is present at distance d, the power reflected back to the receiver in a monostatic radar is [7]

$$P_r = \frac{P_t A_e \sigma}{(4\pi)^2 d^4} \,, \tag{2.2}$$

where A_e is the effective area of the receive antenna and σ the radar cross section (RCS) of the reflecting object. The latter accounts for scattering effects. Equation (2.2) relates the receive power inversely proportional to the fourth power of the distance d. In a bistatic setup, d^4 is replaced $d_1^2 d_2^2$, where d_1 denotes the distance from the transmit antenna to the object and d_2 the distance from the object to the receive antenna. Hence, if σ is assumed to be known, the distance between transmitter and object can be estimated from the measured amplitude of the received signal. For this matter, it is a logical choice to transmit a signal with constant envelope. In practice, σ is often unknown and requires a statistical description, which renders the ranging based on the amplitude model rather difficult. In Chapter 6, this problem is tackled by finding an "average" RCS. Furthermore, a practical wireless channel is subject to multipath propagation. Due to constructive and destructive superposition of the multipath components, the reflected power P_r does not decrease monotonically with increasing distance d.
Because of the uncertainty of the RCS and multipath propagation, the amplitude model is more likely to be found in detection problems, where solely the presence of an object is of interest. In that case, the amplitude of the received signal might be compared to a threshold in order to infer information about the objects presence.

Time of Flight Model (ToF)

The time τ an electro-magnetic wave needs to travel from the transmitter to the object and back in free space is

$$\tau = \frac{2d}{c_0} \,, \tag{2.3}$$

where c_0 denotes the speed of light. In a bistatic setup the numerator is replaced by $d_1 + d_2$. Here, d is estimated from the measured time τ. In contrast to the amplitude model, where a constant envelope signal is used, a pulsed signal has to be used for ToF estimation, in order to define the start and the end of a transmission. In an ideal scenario, the reflected signal is simply a time shifted and attenuated replica of the transmit signal. Correlation of transmitted and the received signal gives information about the time lag τ. Consequently, the distance d can be estimated. Indeed, in the ideal situation where the transmission channel and the RCS are not frequency selective and only additive white Gaussian noise is present, correlation is the optimal mathematical operation. However, in most practical scenarios, especially in indoor environments, multipath propagation causes the transmission channel to be frequency selective and, thus, the reflected signal does not only get attenuated but also distorted. In this case, an optimal estimator has to

account for the effects of the channel. The ability to separate the received multipath echos from each other and, consequently, to determine the one that corresponds to the distance d, is given by the length of the transmitted pulse. Therefore, the accuracy of ToF estimation is essentially limited by the available bandwidth of the system and the channel characteristics, as shown in Chapter 6.

Angle of Arrival Model (AoA)

Under the use of multiple antennas, the direction from the transmitter to the object can be estimated by investigating the time difference of the the signals arriving at the spatially separated antennas. In many cases, this time difference is determined from the phase difference of the continuous wave (CW) carrier. Figure 2.1 pictures the underlying geometry, where the angle of arrival is

$$\varphi_{AoA} = \cos\left(\frac{\Delta d}{d_{Rx}}\right) . \tag{2.4}$$

It should be noted that φ_{AoA} is not defined uniquely in the case of a linear antenna array, where all antennas are arranged on one axis. Horizontal mirroring of Figure 2.1 leads to the same distance Δd from a different angle of arrival. If Δd is derived from the phase difference of the CW carrier and the antenna spacing is larger than half the carrier wavelength, further ambiguity is introduced by the periodicity of the CW carrier.
Estimation of the phase difference between multiple receivers is only possible if they are able to perform coherent detection, i.e., synchronous sampling of the receive signal must be ensured. The discussion of AoA goes through completely analogous for the angle of departure (AoD) with the receive array replaced by the transmit array.

Ranging methods like the amplitude and ToF models are able to estimate the distance to an object on a spherical area. This ambiguity vanishes if multiple transmitters are used. The point on the sphere is then defined by means of trilateration, where the interception of the spheres is calculated. Figure 2.2a depicts the problem in two dimensions.
Figure 2.2b shows the localization of an object by a ranging method combined with AoD and AoA estimation, again, in two dimensions. Ambiguity is reduced to two points in the plane (due to the horizontal symmetry in Figure 2.1).

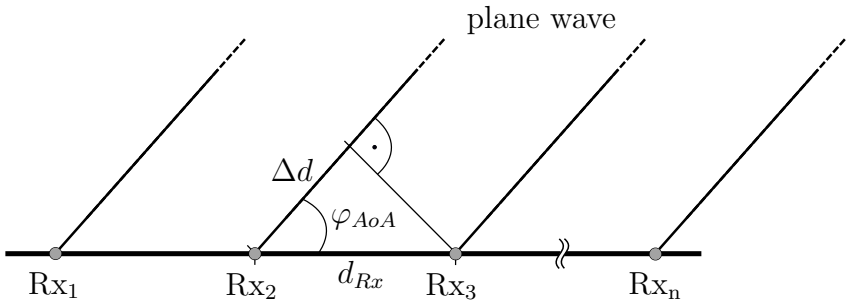

Figure 2.1: Geometry of angle of arrival estimation on a linear antenna array.

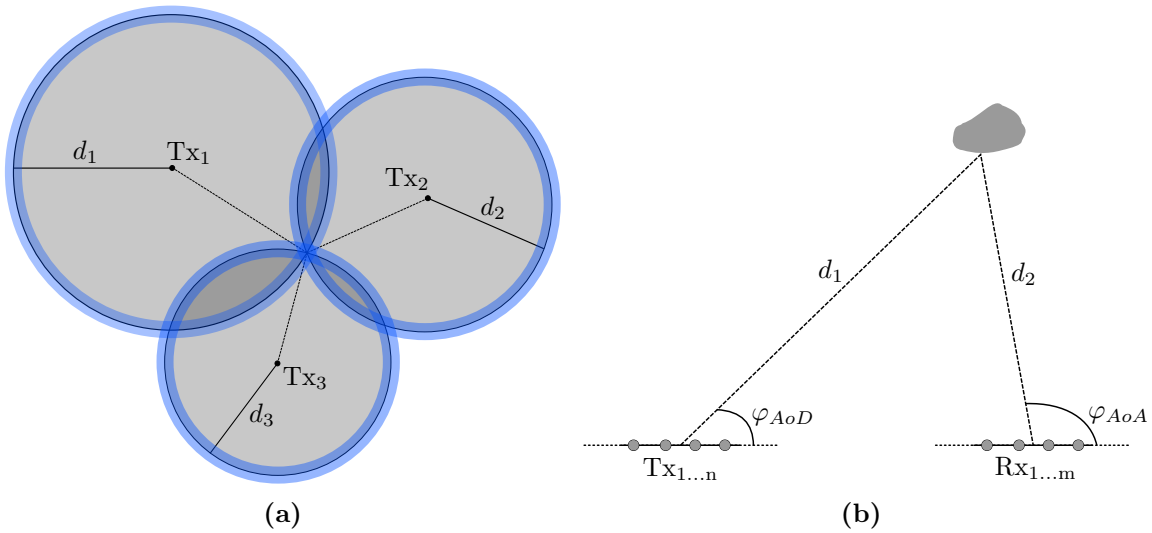

Figure 2.2: **(a)** Trilateration for monostatic radars in two dimensions. Circles become ellipses for bistatic radars. Blue shades symbolize the estimation uncertainty. **(b)** Range, AoD, and AoA estimation in two dimensions.

2.3 Parameter Estimation Theory

In order to gain information about the position of an object, a radar system measures a signal, generally expressed by a random vector $\boldsymbol{y}$. This quantity, also called the *observed vector*, or solely the *observation*, is related to the parameter of interest $\boldsymbol{\theta}$, e.g., the distance to an object, through a physical model. Given the observation $\boldsymbol{y}$, it is the task of parameter estimation to find a formulation for that model and infer knowledge about the parameter $\boldsymbol{\theta}$.

The field of parameter estimation can be divided into deterministic and probabilistic methods. In a deterministic method, the observed vector $\boldsymbol{y}$ is random, but no statistical description is used in order to formulate an estimator. A prominent example is given by the least squares estimator.
In comparison, probabilistic methods are built on statistical descriptions and follow two main philosophies, called *Bayesian* and *classical estimation* [10],[11]. Whereas in the Bayesian framework both, the observations $\boldsymbol{y}$ and the parameter $\boldsymbol{\theta}$ are modeled to be random, the classical framework treats the observations $\boldsymbol{y}$ as random, but the parameter $\boldsymbol{\theta}$ as deterministic vectors. It shall be noted here, that the non-probabilistic treatment of the parameter $\boldsymbol{\theta}$ does not mean that they are inherently deterministic in classical estimation. It rather implies that there is no known statistical description of those. Consequently, there is not always a strict distinction between Bayesian and classical estimation theory in literature [10]. However, the following discussion is based on the Bayesian framework and the relation to classical estimation will be pointed out explicitly.

2.3.1 Optimum Parameter Estimation

In general it is desirable to formulate an estimator that is optimal with respect to some criterion. It is, however, not always possible to find an optimal estimator that is computationally feasible. This might be due to high dimensionality or complex mathematical

relations between observations and parameters. For that matter, this section deals with a general formulation of optimum Bayesian estimators [10], and Sections 2.3.2 and 2.3.3 discuss two competing methods, given in [12] and [13], which make difficult estimation problems more tractable.

Bayesian estimation theory assumes that both, observed variables $\boldsymbol{y}$ and parameters $\boldsymbol{\theta}$, are random. Hence, a probability density function (pdf) is defined for $\boldsymbol{y}$ and $\boldsymbol{\theta}$ by $f_{\mathbf{y}}(\boldsymbol{y})$ and $f_{\boldsymbol{\theta}}(\boldsymbol{\theta})$ and a joint pfd by $f_{\mathbf{y},\boldsymbol{\theta}}(\boldsymbol{y},\boldsymbol{\theta})$. In order to provide an optimality criterion, a cost function expressed by

$$C(\boldsymbol{\theta},\hat{\boldsymbol{\theta}}) = C(\boldsymbol{e})\,, \tag{2.5}$$

with the estimation error $\boldsymbol{e} = \boldsymbol{\theta} - \hat{\boldsymbol{\theta}}$. The optimum Bayesian estimator is then given by the parameter $\hat{\boldsymbol{\theta}}$ that minimizes the expected cost[2] (also called the Bayes risk)

$$\hat{\boldsymbol{\theta}}(\boldsymbol{y}) = \arg\min_{\hat{\boldsymbol{\theta}}} \left\{ \mathrm{E}\big[C(\boldsymbol{\theta},\hat{\boldsymbol{\theta}})\big] \right\} = \arg\min_{\hat{\boldsymbol{\theta}}} \left\{ \int_{\boldsymbol{y}} \int_{\boldsymbol{\theta}} C(\boldsymbol{\theta},\hat{\boldsymbol{\theta}}) f_{\mathbf{y},\boldsymbol{\theta}}(\boldsymbol{y},\boldsymbol{\theta})\, d\boldsymbol{\theta} d\boldsymbol{y} \right\}, \tag{2.6}$$

where $\mathrm{E}\big[\,\cdot\,\big]$ is the expectation operator. Applying Bayes' rule, (2.6) can be rewritten as

$$\hat{\boldsymbol{\theta}}(\boldsymbol{y}) = \arg\min_{\hat{\boldsymbol{\theta}}} \left\{ \int_{\boldsymbol{y}} \left[\int_{\boldsymbol{\theta}} C(\boldsymbol{\theta},\hat{\boldsymbol{\theta}}) f_{\boldsymbol{\theta}|\mathbf{y}}(\boldsymbol{\theta}|\boldsymbol{y})\, d\boldsymbol{\theta} \right] f_{\mathbf{y}}(\boldsymbol{y})\, d\boldsymbol{y} \right\}. \tag{2.7}$$

Noting that $f_{\mathbf{y}}(\boldsymbol{y}) \geqslant 0$ for all values of $\boldsymbol{y}$ and that the choice of $\hat{\boldsymbol{\theta}}$ does not depend on $f_{\mathbf{y}}(\boldsymbol{y})$, (2.7) is minimized by minimizing the term in brackets, where $f_{\boldsymbol{\theta}|\mathbf{y}}(\boldsymbol{\theta}|\boldsymbol{y})$ is called the *posterior pdf*

$$\hat{\boldsymbol{\theta}}(\boldsymbol{y}) = \arg\min_{\hat{\boldsymbol{\theta}}} \int_{\boldsymbol{\theta}} C(\boldsymbol{\theta},\hat{\boldsymbol{\theta}}) f_{\boldsymbol{\theta}|\mathbf{y}}(\boldsymbol{\theta}|\boldsymbol{y})\, d\boldsymbol{\theta}\,. \tag{2.8}$$

Applying Bayes's rule once more, (2.8) reads

$$\hat{\boldsymbol{\theta}}(\boldsymbol{y}) = \arg\min_{\hat{\boldsymbol{\theta}}} \left\{ \int_{\boldsymbol{\theta}} C(\boldsymbol{\theta},\hat{\boldsymbol{\theta}})\, \frac{f_{\mathbf{y}|\boldsymbol{\theta}}(\boldsymbol{y}|\boldsymbol{\theta}) f_{\boldsymbol{\theta}}(\boldsymbol{\theta})}{f_{\mathbf{y}}(\boldsymbol{y})}\, d\boldsymbol{\theta} \right\}. \tag{2.9}$$

Again, $f_{\mathbf{y}}(\boldsymbol{y}) \geqslant 0$ for all $\boldsymbol{y}$, and independent of $\hat{\boldsymbol{\theta}}$. Hence, the denominator is merely a normalization factor ensuring that the posterior pdf integrates to one. The optimum Bayes estimator with respect to the cost function $C(\boldsymbol{\theta},\hat{\boldsymbol{\theta}})$ is finally

$$\hat{\boldsymbol{\theta}}(\boldsymbol{y}) = \arg\min_{\hat{\boldsymbol{\theta}}} \left\{ \int_{\boldsymbol{\theta}} C(\boldsymbol{\theta},\hat{\boldsymbol{\theta}})\, f_{\mathbf{y}|\boldsymbol{\theta}}(\boldsymbol{y}|\boldsymbol{\theta}) f_{\boldsymbol{\theta}}(\boldsymbol{\theta})\, d\boldsymbol{\theta} \right\}, \tag{2.10}$$

where $f_{\mathbf{y}|\boldsymbol{\theta}}(\boldsymbol{y}|\boldsymbol{\theta})$ is the *likelihood function* and $f_{\boldsymbol{\theta}}(\boldsymbol{\theta})$ is the *prior information* on $\boldsymbol{\theta}$.

[2] Here, the expectation is with respect to $\boldsymbol{y}$ and $\boldsymbol{\theta}$.

MAP and ML Estimator

In order to find an explicit formulation of the optimum Bayes estimator, the cost function $C(\boldsymbol{\theta}, \hat{\boldsymbol{\theta}})$ has to be specified. The most frequently used functions are:

- Squared Error:
$$C_{\mathrm{SE}}(\boldsymbol{\theta}, \hat{\boldsymbol{\theta}}) = \|\boldsymbol{\theta} - \hat{\boldsymbol{\theta}}\|^2 \,, \tag{2.11}$$
- Absolute Error:
$$C_{\mathrm{AE}}(\boldsymbol{\theta}, \hat{\boldsymbol{\theta}}) = \sum_{n=1}^{N} |\theta_n - \hat{\theta}_n| \,, \tag{2.12}$$
- Hit-or-Miss Function:
$$C_{\mathrm{HoM}}(\boldsymbol{\theta}, \hat{\boldsymbol{\theta}}) = \begin{cases} 0, & \|\boldsymbol{\theta} - \hat{\boldsymbol{\theta}}\| < \delta \\ 1, & \|\boldsymbol{\theta} - \hat{\boldsymbol{\theta}}\| > \delta \,, \end{cases} \tag{2.13}$$

where $\|\cdot\|$ is the l_2-norm. Choosing the hit-or-miss function avoids the integration over $\boldsymbol{\theta}$ in (2.10), and therefore tends to lead to a more feasible estimator than the other cost functions. It shall thus be considered in the following.

Inserting (2.13) into (2.7), the inner integral can be rewritten as

$$\int_{-\infty}^{\hat{\boldsymbol{\theta}}-\delta} f_{\boldsymbol{\theta}|\mathbf{y}}(\boldsymbol{\theta}|\boldsymbol{y})\, d\boldsymbol{\theta} + \int_{\hat{\boldsymbol{\theta}}+\delta}^{\infty} f_{\boldsymbol{\theta}|\mathbf{y}}(\boldsymbol{\theta}|\boldsymbol{y})\, d\boldsymbol{\theta} = 1 - \int_{\hat{\boldsymbol{\theta}}-\delta}^{\hat{\boldsymbol{\theta}}+\delta} f_{\boldsymbol{\theta}|\mathbf{y}}(\boldsymbol{\theta}|\boldsymbol{y})\, d\boldsymbol{\theta} \,, \tag{2.14}$$

where it has been used, that $\int_{-\infty}^{\infty} f_{\boldsymbol{\theta}|\mathbf{y}}(\boldsymbol{\theta}|\boldsymbol{y})\, d\boldsymbol{\theta} = 1$. Minimizing the right hand side of (2.14) is equivalent to maximizing

$$\int_{\hat{\boldsymbol{\theta}}-\delta}^{\hat{\boldsymbol{\theta}}+\delta} f_{\boldsymbol{\theta}|\mathbf{y}}(\boldsymbol{\theta}|\boldsymbol{y})\, d\boldsymbol{\theta} \,. \tag{2.15}$$

Now, let $\delta \to 0$, then maximizing (2.15) is achieved by choosing $\hat{\boldsymbol{\theta}}$ exactly such, that $f_{\boldsymbol{\theta}|\mathbf{y}}(\boldsymbol{\theta}|\boldsymbol{y})$ is at its maximum, thus

$$\hat{\boldsymbol{\theta}}_{\mathrm{MAP}}(\boldsymbol{y}) = \arg\max_{\hat{\boldsymbol{\theta}}} \left\{ f_{\boldsymbol{\theta}|\mathbf{y}}(\boldsymbol{\theta}|\boldsymbol{y}) \right\} = \arg\max_{\hat{\boldsymbol{\theta}}} \left\{ f_{\mathbf{y}|\boldsymbol{\theta}}(\boldsymbol{y}|\boldsymbol{\theta}) f_{\boldsymbol{\theta}}(\boldsymbol{\theta}) \right\} \tag{2.16}$$

This estimator is called *maximum a posteriori* (MAP) estimator because it maximizes the posterior pdf. For distributions of the exponential family it is often desirable to use the logarithm of the pdf, which is valid because it is a strictly monotonic function

$$\hat{\boldsymbol{\theta}}_{\mathrm{MAP}}(\boldsymbol{y}) = \arg\max_{\hat{\boldsymbol{\theta}}} \left\{ \ln\{ f_{\mathbf{y}|\boldsymbol{\theta}}(\boldsymbol{y}|\boldsymbol{\theta}) f_{\boldsymbol{\theta}}(\boldsymbol{\theta}) \} \right\} = \arg\max_{\hat{\boldsymbol{\theta}}} \left\{ \ln f_{\mathbf{y}|\boldsymbol{\theta}}(\boldsymbol{y}|\boldsymbol{\theta}) + \ln f_{\boldsymbol{\theta}}(\boldsymbol{\theta}) \right\} . \tag{2.17}$$

If the prior pdf $f_{\boldsymbol{\theta}}(\boldsymbol{\theta})$ is unknown, it is often assumed to be uniform over the range of $\boldsymbol{\theta}$. In this case $f_{\boldsymbol{\theta}}(\boldsymbol{\theta})$ is just a constant factor in (2.16) and, consequently,

$$\hat{\boldsymbol{\theta}}_{\mathrm{ML}}(\boldsymbol{y}) = \arg\max_{\hat{\boldsymbol{\theta}}} \left\{ f_{\mathbf{y}|\boldsymbol{\theta}}(\boldsymbol{y}|\boldsymbol{\theta}) \right\} = \arg\max_{\hat{\boldsymbol{\theta}}} \left\{ \ln f_{\mathbf{y}|\boldsymbol{\theta}}(\boldsymbol{y}|\boldsymbol{\theta}) \right\}, \tag{2.18}$$

called the *maximum likelihood* (ML) estimator, because it maximizes the likelihood function.
This ML estimator is equivalent to the ML estimator in classical estimation theory. It should be noted, however, that they are derived in a different context. Whereas in classical estimation the likelihood function is parameterized by the deterministic parameter $\boldsymbol{\theta}$, in the Bayesian framework it is the pdf of $\boldsymbol{y}$ conditioned on $\boldsymbol{\theta}$. Furthermore, the Bayesian ML estimator is evolved from the fact that a certain cost function is used and a noninformative prior pdf is assumed and, therefore, it is a special case of the optimum Bayesian estimator.

2.3.2 Variational Inference Methods

The previous section shows that the general optimum Bayesian estimator (2.7) is found by minimization of the expected cost $C(\boldsymbol{\theta}, \hat{\boldsymbol{\theta}})$ with respect to the posterior pdf $f_{\boldsymbol{\theta}|\mathbf{y}}(\boldsymbol{\theta}|\boldsymbol{y})$. In the case of the hit-or-miss cost function (2.13), optimal estimation is achieved by maximizing $f_{\boldsymbol{\theta}|\mathbf{y}}(\boldsymbol{\theta}|\boldsymbol{y})$ directly. In general, these optimizations are difficult problems, mainly out of the following two reasons: (i) If the parameter is high-dimensional, optimization with respect to $\boldsymbol{\theta}$ is computationally expensive. (ii) If $\boldsymbol{\theta}$ is a continuous variable, the expectation is evaluated by an integral, which might have no closed form solution.
The key to these problems is often found in approximation schemes. There are two concepts that have been subject to extensive research [12],[13] and are used in a variety of problems, namely *variational inference* and *Monte Carlo methods*.

The basic idea of variational inference methods is to narrow down the search space of the original problem. This is done by forcing the approximation to be of a particular form. In order to apply this thought to the Bayesian estimator (2.8), a function $q(\boldsymbol{\theta})$ shall approximate the posterior pdf $f_{\boldsymbol{\theta}|\mathbf{y}}(\boldsymbol{\theta}|\boldsymbol{y})$. A measure for the approximation "quality" is given by the *Kullback-Leibler divergence* (KL divergence) between $q(\boldsymbol{\theta})$ and $f_{\boldsymbol{\theta}|\mathbf{y}}(\boldsymbol{\theta}|\boldsymbol{y})$

$$\mathrm{KL}(q\|f) = -\int_{\boldsymbol{\theta}} q(\boldsymbol{\theta}) \ln\left\{ \frac{f_{\boldsymbol{\theta}|\mathbf{y}}(\boldsymbol{\theta}|\boldsymbol{y})}{q(\boldsymbol{\theta})} \right\} d\boldsymbol{\theta}\,. \tag{2.19}$$

It can be shown that $\mathrm{KL}(q\|f) \geqslant 0$ with equality if and only if $q(\boldsymbol{\theta}) = f_{\boldsymbol{\theta}|\mathbf{y}}(\boldsymbol{\theta}|\boldsymbol{y})$ and that it is not commutative, i.e., $\mathrm{KL}(q\|f) \neq \mathrm{KL}(f\|q)$ [12]. To get a more general view, the following decomposition of the joint distribution is introduced

$$\ln f_{\boldsymbol{\theta},\mathbf{y}}(\boldsymbol{\theta}, \boldsymbol{y}) = \ln f_{\boldsymbol{\theta}|\mathbf{y}}(\boldsymbol{\theta}|\boldsymbol{y}) + \ln f_{\mathbf{y}}(\boldsymbol{y})\,. \tag{2.20}$$

The logarithm of the marginal distribution of $f_{\mathbf{y}}(\boldsymbol{y})$ can be written as

$$\begin{aligned}\ln f_{\mathbf{y}}(\boldsymbol{y}) = &\int_{\boldsymbol{\theta}} q(\boldsymbol{\theta}) \left(\ln f_{\boldsymbol{\theta}|\mathbf{y}}(\boldsymbol{\theta}|\boldsymbol{y}) + \ln f_{\mathbf{y}}(\boldsymbol{y}) - \ln q(\boldsymbol{\theta})\right) d\boldsymbol{\theta} \\ &- \int_{\boldsymbol{\theta}} q(\boldsymbol{\theta}) \left(\ln f_{\boldsymbol{\theta}|\mathbf{y}}(\boldsymbol{\theta}|\boldsymbol{y}) - \ln q(\boldsymbol{\theta})\right) d\boldsymbol{\theta} \,.\end{aligned} \tag{2.21}$$

Inserting (2.20) into (2.21) leads to

$$\ln f_{\mathbf{y}}(\boldsymbol{y}) = \int_{\boldsymbol{\theta}} q(\boldsymbol{\theta}) \ln\left\{\frac{f_{\boldsymbol{\theta},\mathbf{y}}(\boldsymbol{\theta},\boldsymbol{y})}{q(\boldsymbol{\theta})}\right\} d\boldsymbol{\theta} - \int_{\boldsymbol{\theta}} q(\boldsymbol{\theta}) \ln\left\{\frac{f_{\boldsymbol{\theta}|\mathbf{y}}(\boldsymbol{\theta}|\boldsymbol{y})}{q(\boldsymbol{\theta})}\right\} d\boldsymbol{\theta} \,. \tag{2.22}$$

The second term on the right hand side, including the minus sign, is the KL divergence between $q(\boldsymbol{\theta})$ and $f_{\boldsymbol{\theta}|\mathbf{y}}(\boldsymbol{\theta}|\boldsymbol{y})$. Recalling that $\mathrm{KL}(q\|f) \geqslant 0$, with equality if and only if $q(\boldsymbol{\theta}) = f_{\boldsymbol{\theta}|\mathbf{y}}(\boldsymbol{\theta}|\boldsymbol{y})$ implies, that the first integral forms a lower bound on $\ln f_{\mathbf{y}}(\boldsymbol{y})$. In compact notation, (2.22) reads

$$\ln f_{\mathbf{y}}(\boldsymbol{y}) = \mathcal{L}(q) + \mathrm{KL}(q\|f) \tag{2.23}$$

The lower bound $\mathcal{L}(q)$ can also be interpreted as a negative KL divergence, and is therefore always less than or equal to zero. It is concluded, that minimizing the KL divergence $\mathrm{KL}(q\|f)$ is equivalent to maximizing the lower bound $\mathcal{L}(q)$, which is achieved if $q(\boldsymbol{\theta}) = f_{\boldsymbol{\theta},\mathbf{y}}(\boldsymbol{\theta},\boldsymbol{y})$.
However, it is assumed that this is too difficult without restricting $q(\boldsymbol{\theta})$. In the context of *mean field variational inference* [12], $q(\boldsymbol{\theta})$ is modeled to factorize according to

$$q(\boldsymbol{\theta}) = \prod_{i=1}^{N} q_i(\boldsymbol{\theta}_i) \,, \tag{2.24}$$

where $\boldsymbol{\theta}_i$ are disjoint subsets of the vector parameter $\boldsymbol{\theta}$. Using this factorization in the lower bound, it becomes

$$\begin{aligned}\mathcal{L}(q) &= \int_{\boldsymbol{\theta}} \prod_{i=1}^{N} q_i(\boldsymbol{\theta}_i) \ln\left\{\frac{f_{\boldsymbol{\theta},\mathbf{y}}(\boldsymbol{\theta},\boldsymbol{y})}{\prod_{i=1}^{N} q_i(\boldsymbol{\theta}_i)}\right\} d\boldsymbol{\theta} \\ &= \int_{\boldsymbol{\theta}} \left[\prod_{i=1}^{N} q_i(\boldsymbol{\theta}_i)\right] \left[\ln f_{\boldsymbol{\theta},\mathbf{y}}(\boldsymbol{\theta},\boldsymbol{y}) - \sum_{i=1}^{N} \ln q_i(\boldsymbol{\theta}_i)\right] d\boldsymbol{\theta} \\ &= \int_{\boldsymbol{\theta}_j} q_j(\boldsymbol{\theta}_j) \left[\int_{\boldsymbol{\theta}_i} \ln f_{\boldsymbol{\theta},\mathbf{y}}(\boldsymbol{\theta},\boldsymbol{y}) \prod_{i\neq j} q_i(\boldsymbol{\theta}_i) d\boldsymbol{\theta}_i\right] d\boldsymbol{\theta}_j - \int_{\boldsymbol{\theta}_j} q_j(\boldsymbol{\theta}_j) \ln q_j(\boldsymbol{\theta}_j)\, d\boldsymbol{\theta}_j \\ &\quad - \int_{\boldsymbol{\theta}_i} \prod_{i\neq j} q_i(\boldsymbol{\theta}_i) \sum_{i\neq j} \ln q_i(\boldsymbol{\theta}_i) d\boldsymbol{\theta}_i \,.\end{aligned} \tag{2.25}$$

Now, if all $\boldsymbol{\theta}_{i\neq j}$ are kept at a fixed value and $\mathcal{L}(q)$ is maximized only with respect to $\boldsymbol{\theta}_j$, the last integral acts as a constant additive term. The integral inside the brackets is defined as the expectation of the logarithmic joint pdf $\ln f_{\boldsymbol{\theta},\mathbf{y}}(\boldsymbol{\theta},\boldsymbol{y})$ under the approximation $q_{i\neq j}(\boldsymbol{\theta}_{i\neq j})$

$$\mathrm{E}_{i\neq j}\big[\ln f_{\boldsymbol{\theta},\mathbf{y}}(\boldsymbol{\theta},\boldsymbol{y})\big] \coloneqq \int_{\boldsymbol{\theta}_i} \ln f_{\boldsymbol{\theta},\mathbf{y}}(\boldsymbol{\theta},\boldsymbol{y}) \prod_{i\neq j} q_i(\boldsymbol{\theta}_i)\, d\boldsymbol{\theta}_i \,. \tag{2.26}$$

Thus, $\mathcal{L}(q)$ is rewritten as

$$\mathcal{L}(q) = \int_{\boldsymbol{\theta}_j} q_j(\boldsymbol{\theta}_j) \left(\ln \tilde{f}_{\boldsymbol{\theta},\mathbf{y}}(\boldsymbol{\theta},\boldsymbol{y}) - \ln q_j(\boldsymbol{\theta}_j)\right) d\boldsymbol{\theta}_j + \text{const.}\,, \tag{2.27}$$

where the new pdf $\tilde{f}_{\boldsymbol{\theta},\mathbf{y}}(\boldsymbol{\theta},\boldsymbol{y})$ is defined by the relation

$$\ln \tilde{f}_{\boldsymbol{\theta},\mathbf{y}}(\boldsymbol{\theta},\boldsymbol{y}) = \mathrm{E}_{i\neq j}\big[\ln f_{\boldsymbol{\theta},\mathbf{y}}(\boldsymbol{\theta},\boldsymbol{y})\big] \,. \tag{2.28}$$

The form of (2.27) reveals that that $\mathcal{L}(q)$ is a negative KL divergence, and therefore it is maximized with respect to $\boldsymbol{\theta}_j$ if and only if $q_j(\boldsymbol{\theta}_j)$ is equal to $\mathrm{E}_{i\neq j}\big[\ln f_{\boldsymbol{\theta},\mathbf{y}}(\boldsymbol{\theta},\boldsymbol{y})\big]$. Hence, the optimal solution for the j^{th} factor $q_j^\star(\boldsymbol{\theta}_j)$ is

$$\ln q_j^\star(\boldsymbol{\theta}_j) = \mathrm{E}_{i\neq j}\big[\ln f_{\boldsymbol{\theta},\mathbf{y}}(\boldsymbol{\theta},\boldsymbol{y})\big] \,. \tag{2.29}$$

It is seen that the solution with respect to $\boldsymbol{\theta}_j$ depends on all $\boldsymbol{\theta}_{i\neq j}$. This suggests an iterative procedure, where in each iteration the factors are optimized and updated successively. It shall be noted that the approximation error introduced by such a procedure is due to the form of (2.24) and, thus, it depends on the validity of the factorization. If the subsets $\boldsymbol{\theta}_i$ of the parameter $\boldsymbol{\theta}$ are statistically independent, the factorization corresponds to the true distribution and the solution found by the mean field variational approach is equivalent to the optimum solution.

2.3.3 Monte Carlo Methods

In contrast to the deterministic approach of variational inference, Monte Carlo methods [13] represent a statistical notion to the problem of approximation. Although Monte Carlo techniques lead to approximate results in any practical sense, they give exact results under the assumption of infinite computational power. In order to explain the general idea, the optimum Bayesian estimator in (2.8) is reconsidered

$$\hat{\boldsymbol{\theta}}(\boldsymbol{y}) = \arg\min_{\hat{\boldsymbol{\theta}}} \int_{\boldsymbol{\theta}} C(\boldsymbol{\theta},\hat{\boldsymbol{\theta}}) f_{\boldsymbol{\theta}|\mathbf{y}}(\boldsymbol{\theta}|\boldsymbol{y})\, d\boldsymbol{\theta} \,. \tag{2.30}$$

For some important choices of the cost function $C(\boldsymbol{\theta},\hat{\boldsymbol{\theta}})$, this corresponds to an optimization of the conditional expectation of some function $g(\boldsymbol{\theta})$

$$\mathrm{E}\big[g(\cdot)\big] = \int_{\boldsymbol{\theta}} g(\boldsymbol{\theta}) f_{\boldsymbol{\theta}|\mathbf{y}}(\boldsymbol{\theta}|\boldsymbol{y})\, d\boldsymbol{\theta} \,. \tag{2.31}$$

Again, it is claimed that solving this problem directly is either analytically, or computationally infeasible. It shall be assumed, however, that drawing independent samples $\boldsymbol{\theta}^{(i)}$ from the distribution $f_{\boldsymbol{\theta}|\mathbf{y}}(\boldsymbol{\theta}|\boldsymbol{y})$ and the evaluation of this distribution with respect to the drawn sample is easy. The expectation of $g(\boldsymbol{\theta})$ is then approximated by the sample mean, which becomes exact as $N \to \infty$

$$\bar{g} = \frac{1}{N} \sum_{i=1}^{N} g(\boldsymbol{\theta}^{(i)}) \,. \tag{2.32}$$

In the case of the MAP estimator given in (2.16), the posterior pdf is optimized directly and its sampling approximation is given by

$$f'(\boldsymbol{\theta}|\boldsymbol{y}) = \frac{1}{N} \sum_{i=1}^{N} \delta(\boldsymbol{\theta} - \boldsymbol{\theta}^{(i)}) \,, \tag{2.33}$$

where $\delta(\boldsymbol{\theta} - \boldsymbol{\theta}^{(i)})$ is the Dirac delta function located at the sample $\boldsymbol{\theta}^{(i)}$, drawn from $f_{\boldsymbol{\theta}|\mathbf{y}}(\boldsymbol{\theta}|\boldsymbol{y})$. The approximate estimation $\hat{\boldsymbol{\theta}}(\boldsymbol{y})$ is then found by maximizing $f'(\boldsymbol{\theta}|\boldsymbol{y})$.
If the evaluation of $f_{\boldsymbol{\theta}|\mathbf{y}}(\boldsymbol{\theta}|\boldsymbol{y})$ for a drawn sample is easy, it can also be maximized by

$$\hat{\boldsymbol{\theta}}(\boldsymbol{y}) = \arg\max_{\boldsymbol{\theta}^{(i)}} \left\{ f_{\boldsymbol{\theta}|\mathbf{y}}(\boldsymbol{\theta}^{(i)}|\boldsymbol{y}) \right\} , \qquad i = 1, ..., N \,. \tag{2.34}$$

It is seen from (2.34) and (2.32) that, as long as independent samples can be drawn from the given distribution, the quantity to be optimized can be approximated and the approximation becomes exact as $N \to \infty$. Generating samples from simple distributions like the uniform or Gaussian distribution is readily possible in most computer environments, but the use of sampling methods is usually induced by rather complicated, high dimensional distributions. There are a variety of algorithms that address this problem, most notably *rejection sampling*, *importance sampling* and *Markov Chain Monte Carlo* [13]. A discussion of these algorithms is not within the scope of this work, because it builds on the variational inference approach. Nevertheless, it shall be mentioned that, unlike variational inference, these algorithms, with the exception of Markov Chain Monte Carlo, do not scale well with dimensionality [12]. Furthermore, a proposal distribution from which the samples are drawn is needed. It is not always easy to find a well matching distribution and therefore, sampling might be inefficient. On the other hand, if large computational power is available, Monte Carlo techniques lead to results close to the optimum. In view of the presumption, that this is not always the case in environments that are of interest for this work, the remainder of the text is based on the variational inference approach.

3 RFID Localization Algorithms

It is seen from Section 2.1 and 2.2 that radar and RFID systems share a common architectural structure. This similarity renders radar techniques very useful in RFID localization. However, due to several limitations given by the design of RFID systems, it is difficult to apply these techniques to standard off-the-shelf systems. Thus, a novel method developed in [8] is used, which places a dedicated radar signal on top of an existing RFID system. A discussion of this method is given in Section 3.1. Section 3.2 models the RFID backscatter channel, and Section 3.3 explains two algorithms for range and direction estimation. In the first approach, a reduced channel model is assumed, leading to a very simple estimator. Successively, a more elaborate channel model and the information of multiple antennas are used.

3.1 Radar over RFID

As already discussed in Section 2.1, systems following the EPC Class-1 Gen-2 UHF RFID standard [14] use passive backscattering for the tag-to-reader communication. For that matter the reader continues transmitting the unmodulated RF carrier after the query, and the tag answers by modulating its reflection coefficient, thereby varying the amplitude of the signal reflected back to the reader.
Applying localization techniques to the RFID communication itself suffers from various limitations. The amplitude model in (2.2) relies on the RCS of the tag, which strongly depends on the manufacturer and is unknown in general [8]. The accuracy of ToF estimation methods depends on the available bandwidth, which is too low in conventional RFID systems. In order to solve these problems, a low power, direct sequence spread spectrum (DSSS) signal is superimposed onto the RF carrier during the tag to reader communication. This enables the employment of a signal that is suitable for high accuracy range estimation without violating the spectral requirements of the underlying RFID standard.

Figure 3.1 shows an RFID scenario in a multipath environment. The impulse responses of the transmit and receive antennas are given by $h_{tx}(t)$ and $h_{rx}(t)$, respectively, and $h_{cpl}(t)$ describes the mutual coupling. The downlink and uplink channels are denoted by $h_{dl}(t)$ and $h_{ul}(t)$. It should be noted that the multipath components are not termed explicitly, but are included in the down- and uplink. As the tag modulates its impedance for data

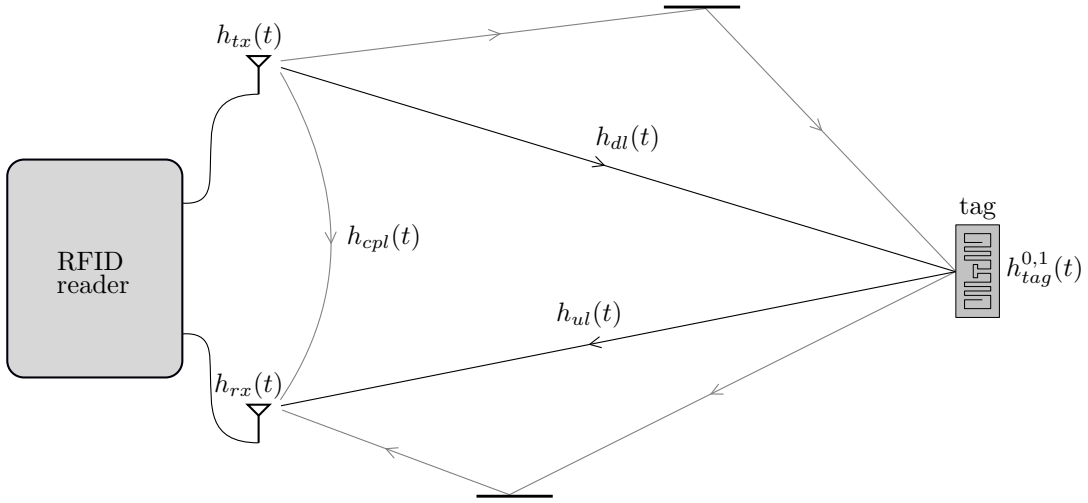

Figure 3.1: Basic RFID scenario. A bistatic setup is shown, where separate antennas are used for transmission and reception.

transmission, $h_{tag}^0(t)$ and $h_{tag}^1(t)$ account for both modulation states.
For the purpose of convenience, in what follows, a bit transmitted by the tag for data communication will be referred to as modulation bit and should not be confused with a chip of the DSSS signal.

The cyclic DSSS baseband signal, which is superimposed onto the RF carrier during the tag to reader communication, is

$$s(t) = 1 + a s_{dsss}(t \bmod T_{dsss}) \,, \tag{3.1}$$

where a is the amplitude, $s_{dsss} \in \{-1, 1\}$, and mod is the modulo function. For reasons that will become apparent presently, the length of one cycle T_{dsss} is chosen to match exactly the duration of one modulation bit minus a fixed guard time T_g. Using the channel model from above, the receive signal is

$$r(t) = \Big(\big[h_{cpl} + h_{dl} * h_{tag}^{m(t)} * h_{ul} \big] * s * h_{tx} * h_{rx} \Big)(t) + w(t) \,, \tag{3.2}$$

with $w(t)$ denoting the receiver noise, $m(t) \in \{0, 1\}$ the modulation state, and "$*$" is the symbol for convolution. During every modulation bit one cycle of the DSSS signal is received, but since the timing of the tags data transmission is unknown, the start of a bit and the start of a cycle do not coincide in general. Exploiting the periodicity of $s(t)$, an alignment can be done by a circular shift as pictured in Figure 3.2. The guard time T_g is inserted to prevent from intersymbol interference. The aligned signal during the k^{th} modulation bit is then

$$r'_k(\tau) = \Big(\big[h_{cpl} + h_{dl} \circledast h_{tag}^{m[k]} \circledast h_{ul} \big] \circledast s \circledast h_{tx} \circledast h_{rx} \Big)(\tau) + w(\tau) \,, \tag{3.3}$$

where $m[k]$ is the decoded modulation state, $\tau = [0, T_{dsss}[$, and "$\circledast$" is the symbol for circular convolution with the cycle length T_{dsss}. Assuming the same number K of 0- and

1-modulation bits and subtracting the average DSSS receive signal during all 1-modulation bits from the average during all 0-modulation bits, the new signal is

$$r_{avg}(\tau) = \frac{1}{K}\sum_{k=1}^{K}\big(1-2m[k]\big)r'_k(\tau)\,. \tag{3.4}$$

Inserting (3.3) into (3.4) and assuming time-invariant impulse responses, it reads

$$\begin{aligned} r_{avg}(\tau) &= \frac{1}{2}\Big(s \circledast h_{tx} \circledast h_{rx} \circledast h_{dl} \circledast h_{ul} \circledast \big[h^0_{tag} - h^1_{tag}\big]\Big)(\tau) + \frac{1}{\sqrt{K}}w(\tau) \\ &= \frac{1}{2}\Big(s \circledast h_{tx} \circledast h_{rx} \circledast h_{dl} \circledast h_{ul} \circledast \Delta h_{tag}\Big)(\tau) + \frac{1}{\sqrt{K}}w(\tau)\,. \end{aligned} \tag{3.5}$$

The factor $1/\sqrt{K}$ stems from the fact that averaging over K recordings reduces the noise power by a factor of $1/K$ in the case of Gaussian noise. Equation (3.5) shows that the coupling $h_{cpl}(\tau)$ between the transmit and the receive antenna is entirely canceled out. For the setup of the system model in Section 3.2 it is assumed that the alignment and averaging is perfectly carried out and, thus, the transmission of the DSSS signal can be seen as a conventional transmission over the channel $h(\tau) = \big(h_{tx} * h_{rx} * h_{dl} * h_{ul} * \Delta h_{tag}\big)(\tau)$.

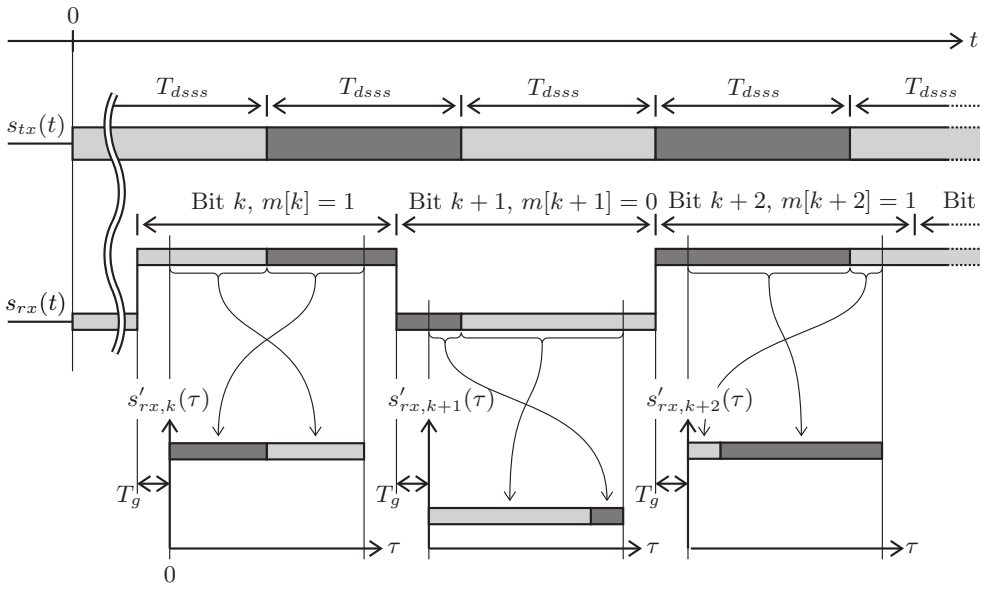

Figure 3.2: Schematic visualization of the procedure to align the DSSS sequence in each received modulation bit [8, Fig. 2]. Due to the cyclic property of the DSSS signal, it can be aligned by a cyclic shift in each modulation bit.

It is emphasized at this point, that such a utilization of a low power DSSS signal with sufficient bandwidth enables the use of ToF estimation techniques while satisfying the spectral mask requirements of the system. Hence, the described method places a localization possibility on top of an existing system without influence on its original purpose. Furthermore, it should be noted that the procedure is not restricted to the EPC UHF RFID standard, but can be applied to any backscatter based RFID system.

3.2 System Model

A basic RFID scenario is depicted in Figure 3.1, where the coupling path $h_{cpl}(t)$ is canceled out by the method described in the previous section. A prerequisite for high accuracy ranging is a representative model of the transmission channel. The characterization and measurement of wireless (backscatter) channels in an indoor environment has been studied intensively, e.g., in [15, 16, 17]. These investigations show that, in addition to a strong line of sight (LOS) component, deterministic multipath components (MPCs), resulting from strong reflections at flat surfaces, as well as diffuse MPCs, originating from scattering effects, are present at the receiver. A more detailed discussion on the transmission channel is given in Chapter 4.
Replacing the transmit and receive antennas in Figure 3.1 by antenna arrays and following the model derived in [18], the backscatter channel from the transmit antenna k to the tag and from the tag back to the receive antenna k' is

$$h_{kk'}(\tau) = \alpha_{kk'}\delta(\tau - \tau_{kk'}) + \nu_{kk'}(\tau)\,, \tag{3.6}$$

where $\delta(\tau)$ is the Dirac delta function, $\alpha_{kk'}$ is the complex amplitude of the LOS component and $\nu_{kk'}(\tau)$ accounts for both, deterministic and diffuse MPCs. Modeling the LOS component by a Dirac pulse implies that the tag has an ideal impulse response, i.e., it is frequency-independent. This is not true in practice and has to be corrected at a later point. Furthermore, the impulse responses of the antennas $h_{tx}(t)$ and $h_{rx}(t)$ in (3.2) are ignored for notational convenience and are reintroduced if required.
The time delay of the LOS component $\tau_{kk'}$ is proportional to the sum of the downlink and uplink distances

$$\tau_{kk'} = \frac{1}{c_0}\big(d_{dl} + d_{ul}\big) = \frac{1}{c_0}\big(\|\boldsymbol{p}_k - \boldsymbol{p}_{tag}\| + \|\boldsymbol{p}_{tag} - \boldsymbol{p}_{k'}\|\big)\,, \tag{3.7}$$

where $\boldsymbol{p}_k$, $\boldsymbol{p}_{k'}$ and $\boldsymbol{p}_{tag}$ are the position vectors of the transmit antenna, the receive antenna and the tag, respectively. This relation is exploited to estimate the distance from the antennas to the tag, as already discussed in Section 2.2.
The receive signal in equivalent baseband notation is given by the convolution of the transmit signal $s(t)$ and the channel $h_{kk'}(t)$

$$r_{kk'}(t) = \alpha_{kk'}s(t - \tau_{kk'})\exp\{-j(2\pi f_c\tau_{kk'} + \Delta\phi)\} + \big(s * \nu_{kk'}\big)(t) + w(t)\,, \tag{3.8}$$

where $w(t)$ is zero mean additive white Gaussian noise (AWGN) and f_c is the carrier frequency. $\Delta\phi$ is the difference between the initial phases of the transmit and the receive local oscillators (LO). This phase difference is also present in the second term of (3.8), but due to the random nature of the multipath $\nu(t)$, it can be ignored. It is important to note that the estimation of the delay $\tau_{kk'}$ is only feasible if the system provides coherent sampling, i.e., synchronization of transmitter and receiver. In the following, it is assumed that synchronization of both the samplers and the LOs is possible and, thus, $\Delta\phi$ can be omitted.
If the received signal is sampled with sampling frequency $f_s = \frac{1}{T_s}$, it can be written in vector notation as

$$\boldsymbol{r}_{kk'} = \alpha_{kk'}\boldsymbol{s}_{\tau_{kk'}} + \boldsymbol{n}_{kk'} + \boldsymbol{w}_{kk'} \,, \tag{3.9}$$

with the sampled versions of the cyclically delayed and phase shifted signal

$$\boldsymbol{s}_{\tau_{kk'}} = \Big[s\big(-\tau_{kk'}\big), s\big(T_s - \tau_{kk'}\big), ..., s\big((N-1)T_s - \tau_{kk'}\big)\Big]^T \exp\{-j2\pi f_c \tau_{kk'}\} \,, \tag{3.10}$$

the circular convolution[1] of the signal and the multipath

$$\boldsymbol{n}_{kk'} = \Big[\big(s \circledast \nu_{kk'}\big)(0), \big(s \circledast \nu_{kk'}\big)(T_s), ..., \big(s \circledast \nu_{kk'}\big)((N-1)T_s)\Big]^T \,, \tag{3.11}$$

and the noise

$$\boldsymbol{w}_{kk'} = \Big[w_{kk'}(0), w_{kk'}(T_s), ..., w_{kk'}((N-1)T_s)\Big]^T \,. \tag{3.12}$$

3.3 Range Estimation

In order to estimate the range[2] between the antennas and the tag, the system model from above is applied to the optimal estimator derived in Chapter 2. In a first consideration the multipath is ignored, which leads to a very simple estimator. In the next step, a more sophisticated estimator is formulated that takes the multipath contribution into account and makes use of the multiple input multiple output (MIMO) information provided by the antenna arrays.

3.3.1 Matched Filter Estimation

The maximum likelihood estimator (2.18) is given by

$$\hat{\boldsymbol{\theta}}(\boldsymbol{y}) = \arg\max_{\hat{\boldsymbol{\theta}}} \left\{ f_{\mathbf{y}|\boldsymbol{\theta}}(\boldsymbol{y}|\boldsymbol{\theta}) \right\} . \tag{3.13}$$

Applying the model (3.9), the estimator for the parameter $\boldsymbol{\theta}_{kk'}$ is

$$\hat{\boldsymbol{\theta}}_{kk'}(\boldsymbol{r}_{kk'}) = \arg\max_{\boldsymbol{\theta}_{kk'}} \left\{ f_{\mathbf{r}_{kk'}|\boldsymbol{\theta}_{kk'}}(\boldsymbol{r}_{kk'}|\boldsymbol{\theta}_{kk'}) \right\} . \tag{3.14}$$

Assuming now, that there is only a LOS component with real, positive $\alpha_{kk'}$, and noise present, i.e., there is *no mulitpath*, the likelihood function is solely dependent on $\tau_{kk'}$

[1] The circular convolution is induced by the alignment procedure (3.3).

[2] Because the range is proportional to the delay τ, the reader should always keep in mind, that, whenever one of those terms is used, it is directly coupled to the other via (3.7).

$$\begin{aligned} f_{\mathbf{r}_{kk'}|\boldsymbol{\tau}_{kk'}}(\boldsymbol{r}_{kk'}|\tau_{kk'}) &= f_{\boldsymbol{\alpha}_{kk'}\boldsymbol{s}_{\tau_{kk'}}+\mathbf{n}_{kk'}|\boldsymbol{\tau}_{kk'}}(\boldsymbol{r}_{kk'}|\tau_{kk'}) \\ &= f_{\mathbf{n}_{kk'}|\boldsymbol{\tau}_{kk'}}(\boldsymbol{r}_{kk'} - \alpha_{kk'}\boldsymbol{s}_{\tau_{kk'}}|\tau_{kk'}) \,. \end{aligned} \tag{3.15}$$

This is simply the pdf of the zero mean AWGN with the argument $\boldsymbol{r}_{kk'} - \alpha_{kk'}\boldsymbol{s}_{\tau_{kk'}}$, conditioned on the parameter $\tau_{kk'}$. It can further be written as

$$\begin{aligned} f_{\mathbf{r}_{kk'}|\boldsymbol{\tau}_{kk'}}(\boldsymbol{r}_{kk'}|\tau_{kk'}) &= f_{\boldsymbol{n}_{kk'}|\boldsymbol{\tau}_{kk'}}(\boldsymbol{r}_{kk'} - \alpha_{kk'}\boldsymbol{s}_{\tau_{kk'}}|\tau_{kk'}) \\ &= \frac{1}{\left(\sqrt{\pi N_0}\right)^N} \exp\Big\{ -\frac{1}{N_0}(\boldsymbol{r}_{kk'} - \alpha_{kk'}\boldsymbol{s}_{\tau_{kk'}})^H(\boldsymbol{r}_{kk'} - \alpha_{kk'}\boldsymbol{s}_{\tau_{kk'}})\Big\} \\ &= \frac{1}{\left(\sqrt{\pi N_0}\right)^N} \exp\Big\{ -\frac{1}{N_0}\big(\|\boldsymbol{r}_{kk'}\|^2 + \alpha_{kk'}\|\boldsymbol{s}_{\tau_{kk'}}\|^2 - 2\alpha_{kk'}\boldsymbol{r}_{kk'}^H\boldsymbol{s}_{\tau_{kk'}}\big)\Big\} \,, \end{aligned} \tag{3.16}$$

where $N_0/2$ is defined to be the two-sided noise power spectral density. Taking the logarithm of (3.16) and inserting it into (3.14) gives

$$\begin{aligned} \hat{\tau}_{kk'}(\boldsymbol{r}_{kk'}) &= \arg\max_{\tau_{kk'}} \Big\{ -\frac{1}{N_0}\big(\|\boldsymbol{r}_{kk'}\|^2 + \alpha_{kk'}\|\boldsymbol{s}_{\tau_{kk'}}\|^2 - 2\alpha_{kk'}\boldsymbol{r}_{kk'}^H\boldsymbol{s}_{\tau_{kk'}}\big)\Big\} \\ &= \arg\max_{\tau_{kk'}} \Big\{ \boldsymbol{r}_{kk'}^H\boldsymbol{s}_{\tau_{kk'}} \Big\} \,, \end{aligned} \tag{3.17}$$

where it is used, that the maximization does not depend on $\|\boldsymbol{r}_{kk'}\|$, $\|\boldsymbol{s}_{\tau_{kk'}}\|$, N_0 and $\alpha_{kk'}$. Equation (3.17) is a representation of the well known *matched filter*, which correlates the received signal with the transmit signal and searches for the time difference τ that maximizes the correlation. This derivation shows that the matched filter is optimal in a maximum likelihood sense for the AWGN channel. However, in a practical indoor wireless radio channel, the MPCs can not be ignored and, thus, the matched filter estimation does not lead to optimal results in general.

Implementation

The correlation in the discrete time domain is given by

$$\boldsymbol{g}[\tau] = \boldsymbol{r}_{kk'}^H\boldsymbol{s}_\tau \,, \tag{3.18}$$

where $\boldsymbol{s}_\tau$ is according to (3.10) with $\tau_{kk'}$ replaced by $\tau = 0, T_s, ..., (N-1)T_s$. It is apparent that the smallest shift in time corresponds to the sampling period T_s and, thus, estimation accuracy is fundamentally limited by it. Assuming a sampling frequency of 100 MHz, the sampling period is 10 ns. A signal, traveling through space with the speed of light propagates 3 m during that time interval. Hence, the shift of one sample in (3.18) corresponds to a ranging difference of 3 m, which is not satisfactory for high accuracy applications. This problem can be tackled by interpolation, which is easily implemented by zero padding in the frequency domain.

3.3.2 Iterative Maximum Likelihood Estimation

The matched filter estimator derived in the previous section does not consider multipath components in the system model. Furthermore, it does not make use of the antenna arrays in a combined manner, but treats each received signal separately. In order to correct for these shortcomings, the next section follows a MIMO approach developed in [18].

3.3.2.1 The MIMO Model

Let the signal be transmitted from each transmit antenna k to each receive antenna k', then all KK' receive signals can be combined into one MIMO receive signal vector

$$\boldsymbol{r} = \left[\boldsymbol{r}_{11'}^T, ..., \boldsymbol{r}_{KK'}^T\right]^T, \tag{3.19}$$

and consequently, the MIMO model for the combined receive signal is

$$\boldsymbol{r} = \alpha\boldsymbol{s} + \boldsymbol{n} + \boldsymbol{w}, \tag{3.20}$$

where $\boldsymbol{s}$, $\boldsymbol{n}$, and $\boldsymbol{w}$ are stacked in the same fashion as (3.19). The distances between the antennas in an array are considered to be small enough[3], that the line of sight amplitude $\alpha_{kk'}$ is approximately equal for all kk' and therefore, it can be placed in front of the combined signal vector $\boldsymbol{s}$.
In wideband systems it is common to model the multipath $\nu(\tau)$ as a zero mean complex Gaussian random process [19]. It can be shown that the linear transformation of a Gaussian process is again Gaussian. Consequently, $\boldsymbol{n}$ is a complex Gaussian random process. By the same argumentation, the superposition of two Gaussian processes is again Gaussian, hence, $\boldsymbol{z} = \boldsymbol{n} + \boldsymbol{w}$ is Gaussian. Considering the sampled version of $z(\tau)$, this is written in vector notation as

$$\boldsymbol{z} \sim \mathcal{N}_{NKK'}(\boldsymbol{0}, \boldsymbol{C}). \tag{3.21}$$

The covariance matrix is a block diagonal matrix $\boldsymbol{C} = \mathrm{diag}\{\boldsymbol{C}_{11'}, ..., \boldsymbol{C}_{\mathrm{KK'}}\}$ with

$$\boldsymbol{C}_{kk'} = \boldsymbol{S}^H \boldsymbol{C}_{\nu_{kk'}} \boldsymbol{S} + N_0 \boldsymbol{I}, \tag{3.22}$$

where

$$\boldsymbol{S} = \left[\boldsymbol{s}_0, \boldsymbol{s}_{T_s}, ..., \boldsymbol{s}_{(N-1)T_s}\right]^T \tag{3.23}$$

is the "convolution matrix" of the transmit signal and $\boldsymbol{C}_{\nu_{kk'}}$ is the covariance matrix of the multipath $\boldsymbol{\nu}_{kk'}$. For wideband systems it is often assumed that the multipath components are uncorrelated. In this case, the auto-correlation of the multipath $\nu_{kk'}(\tau)$ is [19]

[3] Compared to the distance between the array and the tag.

$$\mathrm{E}\big[\nu^*_{kk'}(\tau)\nu_{kk'}(\tau')\big] = \rho_{\nu_{kk'}}(\tau)\delta(\tau-\tau')\,, \tag{3.24}$$

where $\rho_{\nu_{kk'}}(\tau)$ is the power delay profile (PDP) of the multipath[4]

$$\rho_{\nu_{kk'}}(\tau) = \lim_{T\to\infty}\frac{1}{2T}\int_{-\infty}^{\infty}|\nu_{kk'}(t,\tau)|^2\,dt \mathrel{\widehat{=}} |\nu_{kk'}(\tau)|^2\,. \tag{3.25}$$

The covariance matrix (3.22) can now be rewritten as

$$\boldsymbol{C}_{kk'} = \boldsymbol{S}^H\mathrm{diag}\{\boldsymbol{\rho}_{\nu_{kk'}}\}\boldsymbol{S} + N_0\boldsymbol{I}, \tag{3.26}$$

with $\boldsymbol{\rho}_{\nu_{kk'}}$ being the sampled version of the PDP of the channel from antenna k to k'.

3.3.2.2 Parameters and Approximations

Considering (3.21) and (3.26), the likelihood function of the combined receive signal (3.20) is

$$\begin{aligned} f_{\mathbf{r}|\boldsymbol{\theta}}(\boldsymbol{r}|\boldsymbol{\theta}) &= f_{\boldsymbol{\alpha}\mathbf{s}+\mathbf{z}|\boldsymbol{\theta}}(\boldsymbol{r}|\boldsymbol{\theta}) \\ &= f_{\mathbf{z}|\boldsymbol{\theta}}(\boldsymbol{r}-\alpha\boldsymbol{s}|\boldsymbol{\theta}) \\ &= \frac{1}{\pi^{NKK'}|\boldsymbol{C}(\boldsymbol{\zeta})|}\exp\Big\{-(\boldsymbol{r}-\alpha\boldsymbol{s}(\boldsymbol{\psi}))^H\boldsymbol{C}(\boldsymbol{\zeta})^{-1}(\boldsymbol{r}-\alpha\boldsymbol{s}(\boldsymbol{\psi}))\Big\}\,, \end{aligned} \tag{3.27}$$

where $|\cdot|$ is the determinant and $\boldsymbol{\theta} = \big[\boldsymbol{\psi}^T, \alpha, \boldsymbol{\zeta}^T\big]^T$ is the NKK'+5 -dimensional parameter vector[5]. $\boldsymbol{\zeta} = \big[\boldsymbol{\nu}^T, N_0\big]^T$, $\boldsymbol{\nu} = \big[\boldsymbol{\nu}_{11'}^T, ..., \boldsymbol{\nu}_{KK'}^T\big]^T$ is the sampled version of the multipath, $\boldsymbol{\psi} = \big[\tau, \varphi_{AoD}, \varphi_{AoA}\big]^T$, φ_{AoD} is the angle of departure, φ_{AoA} is the angle of arrival, and τ is the delay from the center of the transmit array to the tag and from the tag back to the center of the receive array

$$\tau = \frac{1}{c_0}\big(\|\overline{\boldsymbol{p}_k} - \boldsymbol{p}_{tag}\| + \|\boldsymbol{p}_{tag} - \overline{\boldsymbol{p}_{k'}}\|\big)\,. \tag{3.28}$$

In order to unveil the dependence of $\boldsymbol{s}(\boldsymbol{\psi})$ on $\boldsymbol{\psi}$, the definition of $\boldsymbol{s}_{\tau_{kk'}}$ given by (3.10) is reconsidered. Each $\boldsymbol{s}_{\tau_{kk'}}$ contained in $\boldsymbol{s}$ depends on $\tau_{kk'}$. But, given the geometry of the antenna arrays, all delays $\tau_{kk'}$ are in a fixed relation to each other. With the centers of the antenna arrays as reference points, $\boldsymbol{s}_{\tau_{kk'}}$ can be rewritten as

[4] In time varying scenarios, the PDP is the squared absolute value of the channel at delay τ, averaged over the time t. The measurement setup in Chapter 5 describes a static environment, i.e., the multipath does not change over time for a fixed position of the tag. In this case, $\nu_{kk'}(\tau)$ does not depend on t and the integral disappears.

[5] $\tau \in \mathbb{R}_+$; $\varphi_{AoA}, \varphi_{AoD} \in [0, 2\pi]$; $\alpha \in \mathbb{C}$; $\boldsymbol{\nu} \in \mathbb{C}^{NKK'}$; $N_0 \in \mathbb{R}_+$

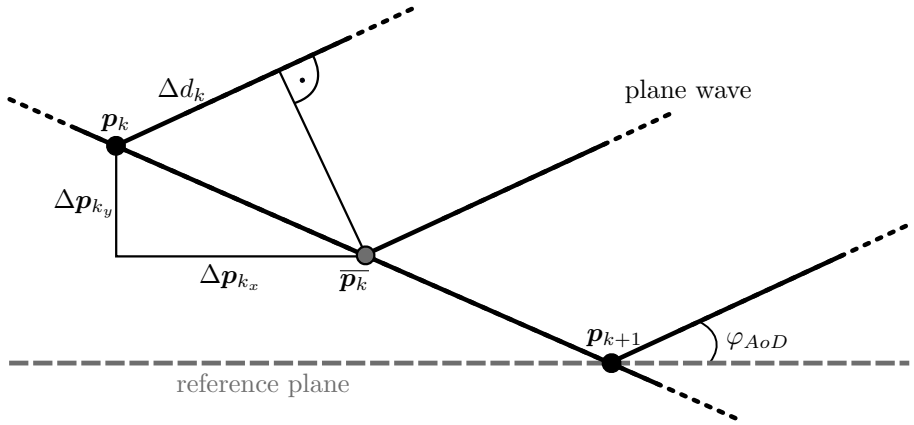

Figure 3.3: Geometric relation between a linear antenna array, the AoD and the delay difference of a plane wave at each antenna. The assumption of a plane wave departing from/arriving at an antenna is only valid, if the distance between tag and antenna array is large, compared to the distances between the antennas of the array.

$$\begin{aligned}\boldsymbol{s}_{\tau_{kk'}} =& \Big[s\big(-(\tau-\Delta\tau_{kk'})\big), s\big(T_s-(\tau-\Delta\tau_{kk'})\big), ..., s\big((N-1)T_s-(\tau-\Delta\tau_{kk'})\big)\Big]^T \\ & \exp\{-j2\pi f_c(\tau-\Delta\tau_{kk'})\}\end{aligned} \tag{3.29}$$

and [20]

$$\begin{aligned}\Delta\tau_{kk'} &= \frac{1}{c_0}\big(\Delta d_k + \Delta d_{k'}\big) \\ &= \frac{1}{c_0}\big(\Delta \boldsymbol{p}_{k_x}\cos(\varphi_{AoD}) + \Delta \boldsymbol{p}_{k_y}\sin(\varphi_{AoD}) \\ &\quad + \Delta \boldsymbol{p}_{k'_x}\cos(\varphi_{AoA}) + \Delta \boldsymbol{p}_{k'_y}\sin(\varphi_{AoA})\big)\,.\end{aligned} \tag{3.30}$$

The parameters in (3.30) are explained in Figure 3.3. Although the scenario is drawn with respect to the angle of departure at the transmit array, it is completely analogous for the angle of arrival at the receive array.
By expressing $\boldsymbol{s}$ in terms of $\boldsymbol{\psi}$ instead of each individual $\tau_{kk'}$, the parameter space is reduced from KK' to three dimensions.

It should be noted at this point, that the primal goal is to estimate the range between the tag and the antennas, which is proportional to the delay τ. All other parameters in $\boldsymbol{\theta} = \left[\boldsymbol{\psi}^T, \alpha, \boldsymbol{\zeta}^T\right]^T$ are not of direct interest to the problem, but have to be estimated alongside the delay. They are called *nuisance parameters*.

The likelihood function (3.27) shall now be minimized. But the parameter $\boldsymbol{\theta}$ is of dimension $NKK' + 5$ and thus, minimization with respect to $\boldsymbol{\theta}$ is difficult. A solution to

this problem is found by applying the approach of mean field variational inference, discussed in Section 2.3.2. Using (2.24), it is assumed that the approximation of the posterior distribution can be factorized by

$$q(\boldsymbol{\theta}) = q(\boldsymbol{\psi})q(\alpha)q(\boldsymbol{\zeta})\,. \tag{3.31}$$

While the parameters $\boldsymbol{\psi}$ and α have dimensions three and one, respectively, the parameter $\boldsymbol{\zeta}$ includes the multipath vector $\boldsymbol{\nu}$, which has dimension NKK'. In this work, the length of the receive signal vectors[6] $\boldsymbol{r}_{kk'}$ is $N = 1022$. This is considered to be too high dimensional for minimization with respect to $\boldsymbol{\zeta}$ directly. In [18], the dimensionality is reduced by parameterizing the PDP of the multipath with only a few parameters and estimating those, instead of the original vector. Here, the covariance matrix $\boldsymbol{C}$ is estimated separately in a sample matrix approach (see Section 3.3.2.5). Therefore, $\boldsymbol{C}$ does not depend on the parameter $\boldsymbol{\zeta}$ anymore and it can thus be ignored in (3.31). Consequently, the factorization of the posterior pdf is rewritten as

$$q(\boldsymbol{\theta}) = q(\boldsymbol{\psi})q(\alpha)\,, \tag{3.32}$$

with $\boldsymbol{\theta} = \left[\boldsymbol{\psi}^T, \alpha\right]^T$.

3.3.2.3 Iterative Parameter Estimation

In (2.29) it is stated that the optimal solution of the logarithm of each factor in (3.32) is the expectation of the logarithmic joint pdf under the product of all other factors $\ln q_j^\star(\boldsymbol{\theta}_j) = \mathrm{E}_{i\neq j}\left[\ln f_{\boldsymbol{\theta},\mathbf{y}}\right]$. The optimal factor with respect to $\boldsymbol{\psi}$ is then

$$\begin{aligned}
\ln q^\star(\boldsymbol{\psi}) &= \mathrm{E}_\alpha\left[\ln f_{\mathbf{r},\boldsymbol{\theta}}\right] \\
&= \int_\alpha \ln f_{\mathbf{r},\boldsymbol{\theta}}(\boldsymbol{r},\boldsymbol{\theta})\, q(\alpha)\, d\alpha \\
&= \int_\alpha \ln f_{\mathbf{r},\boldsymbol{\psi},\alpha}(\mathbf{r},\boldsymbol{\psi},\alpha)\, q(\alpha)\, d\alpha
\end{aligned} \tag{3.33}$$

and the estimated value for $\boldsymbol{\psi}$ is

$$\begin{aligned}
\hat{\boldsymbol{\psi}} &= \arg\max_{\boldsymbol{\psi}} \left\{\ln q^\star(\boldsymbol{\psi})\right\} \\
&= \arg\max_{\boldsymbol{\psi}} \left\{ \int_\alpha \ln f_{\mathbf{r},\boldsymbol{\psi},\alpha}(\boldsymbol{r},\boldsymbol{\psi},\alpha)\, q(\alpha)\, d\alpha \right\}.
\end{aligned} \tag{3.34}$$

Because no information is given about α, a point estimate $q(\alpha) = \delta(\alpha - \hat{\alpha})$ is chosen, where $\hat{\alpha}$ is the estimate of the true parameter α. The equation above simplifies to

[6] The length N is determined by the bandwidth of the DSSS signal and the duration of a modulation bit in the RFID communication (see Section 3.1).

$$\begin{aligned}\hat{\boldsymbol{\psi}} &= \arg\max_{\boldsymbol{\psi}} \left\{ \ln f_{\mathbf{r},\boldsymbol{\psi},\boldsymbol{\alpha}}(\mathbf{r},\boldsymbol{\psi},\hat{\alpha}) \right\} \\ &= \arg\max_{\boldsymbol{\psi}} \left\{ \ln\big(f_{\mathbf{r}|\boldsymbol{\psi},\boldsymbol{\alpha}}(\mathbf{r}|\boldsymbol{\psi},\hat{\alpha}) f_{\boldsymbol{\psi}}(\boldsymbol{\psi})\big) + \ln f_{\boldsymbol{\alpha}}(\hat{\alpha}) \right\}.\end{aligned} \tag{3.35}$$

As no prior information on $\boldsymbol{\psi}$ is available, a (noninformative) uniform pdf is chosen. Finally, the estimator for $\boldsymbol{\psi}$ is the maximum likelihood estimator

$$\begin{aligned}\hat{\boldsymbol{\psi}} &= \arg\max_{\boldsymbol{\psi}} \left\{ \ln f_{\mathbf{r}|\boldsymbol{\psi},\boldsymbol{\alpha}}(\mathbf{r}|\boldsymbol{\psi},\hat{\alpha}) \right\} \\ &= \arg\max_{\boldsymbol{\psi}} \left\{ -\big(\boldsymbol{r} - \hat{\alpha}\boldsymbol{s}(\boldsymbol{\psi})\big)^H \boldsymbol{C}^{-1} \big(\boldsymbol{r} - \hat{\alpha}\boldsymbol{s}(\boldsymbol{\psi})\big) \right\}.\end{aligned} \tag{3.36}$$

The steps (3.33)–(3.36) are completely analogous for α, with the roles of α and ψ being switched. Hence, the estimator for α is

$$\hat{\alpha} = \arg\max_{\alpha} \left\{ -\big(\boldsymbol{r} - \alpha\boldsymbol{s}(\hat{\boldsymbol{\psi}})\big)^H \boldsymbol{C}^{-1} \big(\boldsymbol{r} - \alpha\boldsymbol{s}(\hat{\boldsymbol{\psi}})\big) \right\}, \tag{3.37}$$

where $\hat{\boldsymbol{\psi}}$ is the previously estimated $\boldsymbol{\psi}$. By setting the derivative of the expression inside the curly brackets in (3.37) to zero and solving for α, a closed-form solution for $\hat{\alpha}$ is found

$$\hat{\alpha} = \frac{\boldsymbol{r}^H \boldsymbol{C}^{-1} \boldsymbol{s}(\hat{\boldsymbol{\psi}})}{\boldsymbol{s}(\hat{\boldsymbol{\psi}})^H \boldsymbol{C}^{-1} \boldsymbol{s}(\hat{\boldsymbol{\psi}})}. \tag{3.38}$$

However, (3.36) and (3.38) do not pose an explicit solution, because each of them depends on the estimate of the other parameter. This requires an iterative procedure, shown in Algorithm 3.1, where in every iteration both parameters are estimated in turn. It is important to note, that even though the estimation of the covariance matrix $\boldsymbol{C}$ is not part of the variational inference formulation, it will be seen in Section 3.3.2.5 that it depends on the parameters $\boldsymbol{\psi}$ and α. It is therefore also included in the iterative procedure.

As for every iterative method, initialization, discussed in Section 3.3.2.4, and convergence criteria are important aspects. A possible convergence criterion evaluates how much the estimation of a parameter has changed from the previous to the current iteration and stops the procedure, if the change is smaller than a certain value. Formally, this is expressed by a boolean variable

$$[B_{con}] = \begin{cases} 1, & |\hat{\boldsymbol{\theta}} - \hat{\boldsymbol{\theta}}'| \preceq \boldsymbol{\epsilon} \\ 0, & |\hat{\boldsymbol{\theta}} - \hat{\boldsymbol{\theta}}'| \succ \boldsymbol{\epsilon}, \end{cases} \tag{3.39}$$

Algorithm 3.1: Iterative Maximim Likelihood Estimation

initialize $\hat{\alpha}$ using (3.40)
initialize $\hat{\boldsymbol{\psi}}$ using (3.17) and (3.44)
initialize $\hat{\boldsymbol{C}}$ using (3.46)
convergence criterion $\leftarrow$ `false`
while convergence criterion is `false` **do**
  estimate $\hat{\alpha}$ using (3.38)
  estimate $\hat{\boldsymbol{\psi}}$ using (3.36)
  estimate $\hat{\boldsymbol{C}}$ using (3.46)
  if $|\hat{\boldsymbol{\theta}} - \hat{\boldsymbol{\theta}}'| \preceq \boldsymbol{\epsilon}$ **then**
    convergence criterion $\leftarrow$ `true`
  $\hat{\boldsymbol{\theta}}' \leftarrow \hat{\boldsymbol{\theta}}$

where $\hat{\boldsymbol{\theta}}'$ is the estimate of $\boldsymbol{\theta}$ in the previous iteration and "$\preceq$" is the component-wise inequality, that is $|\theta_i - \theta_i'| \leqslant \epsilon_i, \forall i$. It is obvious, that $\boldsymbol{\epsilon}$ has a strong influence on the convergence behavior and should therefore be chosen with care. While a too large $\boldsymbol{\epsilon}$ might prevent the algorithm from getting close to the true parameter $\boldsymbol{\theta}$, a too small $\boldsymbol{\epsilon}$ forces the algorithm to proceed, although the gain in estimation accuracy is negligible.

3.3.2.4 Initialization

The delay parameter τ and the LOS amplitude α are initialized using the matched filter approach derived in Section 3.3.1. Equation (3.17) can be used directly to estimate the delay $\tau_{kk'}$ from every transmit antenna k to every receive antenna k'. Using linear antenna arrays, τ is geometrically given by the mean of all $\tau_{kk'}$. The complex LOS amplitude $\alpha_{kk'}$ is estimated by the maximum value of the matched filter, that is at $\hat{\tau}_{kk'}$, normalized by the energy of the transmit signal

$$\hat{\alpha}_{kk'} = \frac{\boldsymbol{r}_{kk'}^H \boldsymbol{s}_{\hat{\tau}_{kk'}}}{\boldsymbol{s}^H \boldsymbol{s}} \,, \tag{3.40}$$

where $\boldsymbol{s}_{\hat{\tau}_{kk'}}$ is the transmit signal shifted by $\hat{\tau}_{kk'}$. Analog to the delay τ, $\hat{\alpha}$ is found by calculating the mean of all $\hat{\alpha}_{kk'}$.

For the initialization of the angle of departure φ_{AoD} and angle of arrival φ_{AoA}, the distance differences Δd_k and $\Delta d_{k'}$ (see Figure 3.3) have to be estimated. They are derived from the phase difference of the signal at the elements of the antenna arrays. The carrier phase of the line of sight component from antenna k to antenna k' in (3.29) is

$$\phi_{kk'} = 2\pi f_c(\tau - \Delta\tau_{kk'}) \,. \tag{3.41}$$

A simple estimation approach is, again, given by the matched filter

$$\hat{\phi}_{kk'} = \arg\left\{ \boldsymbol{r}_{kk'}^H \boldsymbol{s}_{\hat{\tau}_{kk'}} \right\} , \tag{3.42}$$

where $\arg\{\cdot\}$ is the argument function. The phase difference between the signal transmitted from antenna k to k' and from antenna l to k' is then

$$\Delta\hat{\phi}_{kl,k'} = \hat{\phi}_{kk'} - \hat{\phi}_{lk'} \,. \tag{3.43}$$

Consequently, the angle of departure can be estimated by

$$\hat{\varphi}_{AoD} = \arg\min_{\varphi_{AoD}} \left\{ \left| \Delta\hat{\phi}_{kl,k'} - \frac{2\pi f_c}{c_0} \left(\Delta \boldsymbol{p}_{x_{kl}} \cos(\varphi_{AoD}) + \Delta \boldsymbol{p}_{y_{kl}} \sin(\varphi_{AoD}) \right) \right| \right\}, \tag{3.44}$$

where $\Delta \boldsymbol{p}_{x_{kl}}$ and $\Delta \boldsymbol{p}_{y_{kl}}$ are the distances between the antenna elements k and l in x- and y-direction. Extension from two to multiple antennas in a linear antenna array is straight forward by, e.g., estimating all phase differences between two consecutive antennas and calculating the mean.

3.3.2.5 Covariance Estimation

In order to formulate an estimator for the covariance matrix $\boldsymbol{C}_{kk'}$, the signal model (3.9) is reconsidered

$$\boldsymbol{r}_{kk'} = \alpha_{kk'} \boldsymbol{s}_{\tau_{kk'}} + \boldsymbol{n}_{kk'} + \boldsymbol{w}_{kk'} \,, \tag{3.45}$$

where $\boldsymbol{C}_{kk'}$ is the covariance of the receive signal without the LOS component $\boldsymbol{r}_{kk'} - \alpha_{kk'} \boldsymbol{s}_{\tau_{kk'}} = \boldsymbol{n}_{kk'} + \boldsymbol{w}_{kk'}$. For a stationary channel, a simple estimator is given by the sample covariance matrix

$$\hat{\boldsymbol{C}}_{kk'} = \frac{1}{M} \sum_{i=1}^{M} \left(\boldsymbol{r}_{kk'}[i] - \alpha_{kk'} \boldsymbol{s}_{\tau_{kk'}} \right) \left(\boldsymbol{r}_{kk'}[i] - \alpha_{kk'} \boldsymbol{s}_{\tau_{kk'}} \right)^H, \tag{3.46}$$

where i denotes the time instance. It is apparent that this estimator depends on the LOS amplitude $\alpha_{kk'}$ and on the delay $\tau_{kk'}$. This requires initialization of those parameters in advance and implies that the estimate $\hat{\boldsymbol{C}}_{kk'}$ has to be updated in every iteration, like it is shown in Algorithm 3.1.
In nonstationary scenarios, where the channel statistics change over time, an exponential forgetting factor is included [21]

$$\hat{\boldsymbol{C}}_{kk'} = (1-\lambda) \sum_{i=1}^{M} \lambda^{M-i} \left(\boldsymbol{r}_{kk'}[i] - \alpha_{kk'} \boldsymbol{s}_{\tau_{kk'}} \right) \left(\boldsymbol{r}_{kk'}[i] - \alpha_{kk'} \boldsymbol{s}_{\tau_{kk'}} \right)^H, \tag{3.47}$$

with $0 < \lambda < 1$.
In [18], the covariance estimation is based on the estimation of the parameterization of the channel PDP. Consequently, the quality of the estimation depends on how well the modeled PDP describes the reality. The advantage of the sample covariance approach is, that it does not depend on such a model, which implies that it is valid for multiple environments with different channel characteristics.

4 Backscatter Channel Modeling

For the evaluation of the range estimation methods in Chapter 3, it is necessary to know the (location specific) behavior of the transmission channel. The practical approach is to perform measurements within the environment where the system is deployed. This poses several difficulties: (i) RF-measurement equipment is expensive. (ii) The equipment might not be able to perform measurements for a wide range of different parameters, such as transmit power, frequency, or bandwidth. (iii) The execution of measurements might be difficult, e.g., due to the transportation of heavy equipment to a (possibly unsuitable) location of the measurement.
An alternative for the characterization of transmission channels is given by means of computer simulations. In theory, the field strength of electro-magnetic waves is determined for every location at any time by Maxwell's equations. The channel behavior can thus be determined in a completely deterministic way by solving these equations. However, this is computationally too expensive for most computer environments. Additionally, the exact boundary conditions for Maxwell's equations are often unknown. A feasible solution to the problem is found by a high frequency approximation. This simplified approach considers electro-magnetic waves to behave like rays, following the laws of geometrical optics, and is therefore also referred to as *ray tracing*. [19]
In Section 4.1, the purely deterministic model of ray tracing is discussed. As this method only considers the specular components, but no diffuse components of a multipath channel, it usually underestimates the true behavior of the channel. This motivates the extension through a statistical description, studied in Section 4.2.

4.1 Ray Tracing

A three dimensional ray tracer simulates the transmission of plane waves in every direction on a sphere around the transmitter. These plane waves propagate towards the receiver, like rays, on a direct line of sight path and a number of paths that are created by one or multiple reflections at flat surfaces. A possible way to identify the paths contributing to the receive signal is to divide the sphere around the receiver into small areas and follow every ray that travels from the transmitter through the center of an area. The path of the ray is then followed until it either reaches the receiver or the attenuation due to reflections and free space propagation loss is too high. This is computationally inefficient, because rays that do not contribute to the receive signal are also considered. A more effective

approach is given by the concept of virtual transmitters. They are calculated by mirroring the location of the transmitter with respect to the reflecting surface. The straight line connecting the virtual transmitter and the receiver is of the same length as the reflected ray and both hit the reflecting surface with the same angle of incidence Θ_i. Figure 4.1 shows an example of virtual transmitters for first and second order reflections.

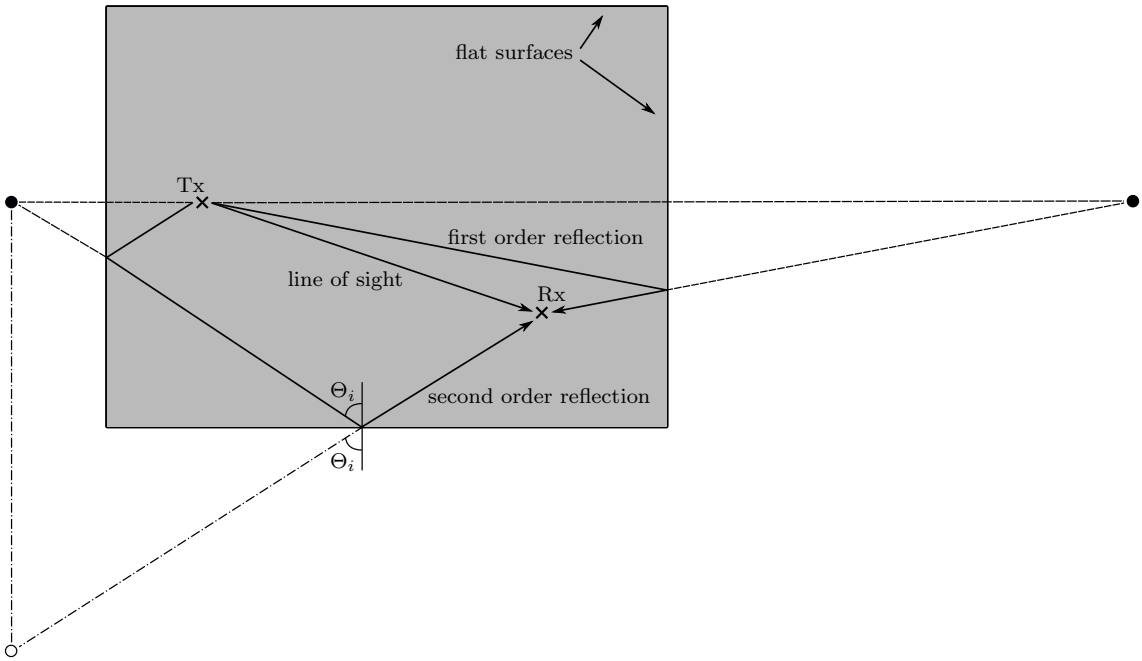

Figure 4.1: Principle of virtual transmitters. Filled circles: virtual transmitters for first order reflections. Empty circles: virtual transmitters for second order reflections. Solid lines: line of sight and actual reflected paths. Dashed and dash-dotted lines: paths from the virtual transmitters to the receiver.

4.1.1 Continuous Wave Description

A continuous plane wave with amplitude a and frequency f_c is described by a complex harmonic function

$$p_{tx}(t) = a \exp\{-j2\pi f_c t\} . \tag{4.1}$$

A wave with amplitude $a = 1$, originating from an isotropically radiating transmitter with constant gain $G_{tx} = 1$, traveling to an isotropic receiver with constant gain $G_{rx} = 1$, on the LOS path of distance d, is attenuated and phase shifted

$$p_{rx}(t, \tau) = \tilde{\alpha} \exp\{-j2\pi f_c (t + \tau)\} , \tag{4.2}$$

where $\tau = \frac{d}{c_0}$ and $\tilde{\alpha}$ is the square root of the free space path loss factor

$$\tilde{\alpha} = \frac{\lambda}{4\pi d} . \tag{4.3}$$

Reflected waves experience, in addition to the free space path loss, attenuations, originating from interactions with the reflecting object. These attenuations are defined by the *reflection* and *transmission coefficients*, which depend on the material properties of the object and on the angle of incidence Θ_i. It is assumed that the relative permeability μ_r is 1 for all considered materials.[1] The materials are then characterized by their dielectric constant ε and conductivity σ_e, combined in the complex dielectric constant [19]

$$\delta = \varepsilon - j\frac{\sigma_e}{2\pi f_c} \,. \tag{4.4}$$

The reflection and transmission coefficients R_{TE} and T_{TE} for transversal electric (TE, a linearly polarized wave with the electric field component parallel to the reflecting surface) waves, at the boundary of two materials with δ_1 and δ_2, are

$$R_{\mathrm{TE}} = \frac{\sqrt{\delta_1}\cos\Theta_i - \sqrt{\delta_2}\cos\Theta_t}{\sqrt{\delta_1}\cos\Theta_i + \sqrt{\delta_2}\cos\Theta_t} \tag{4.5}$$

$$T_{\mathrm{TE}} = \frac{2\sqrt{\delta_1}\cos\Theta_i}{\sqrt{\delta_1}\cos\Theta_i + \sqrt{\delta_2}\cos\Theta_t} \,, \tag{4.6}$$

where Θ_t is the angle between the transmitted wave and the line normal to the reflecting surface. For transversal magnetic (TM, a linearly polarized wave with the magnetic field component parallel to the reflecting surface) waves, the coefficients are

$$R_{\mathrm{TM}} = \frac{\sqrt{\delta_2}\cos\Theta_i - \sqrt{\delta_1}\cos\Theta_t}{\sqrt{\delta_2}\cos\Theta_i + \sqrt{\delta_1}\cos\Theta_t} \tag{4.7}$$

$$T_{\mathrm{TM}} = \frac{2\sqrt{\delta_1}\cos\Theta_i}{\sqrt{\delta_2}\cos\Theta_i + \sqrt{\delta_1}\cos\Theta_t} \,. \tag{4.8}$$

All coefficients can solely be expressed in terms of the incident angle Θ_i by using Snell's law

$$\frac{\sin\Theta_t}{\sin\Theta_i} = \frac{\sqrt{\delta_1}}{\sqrt{\delta_2}} \,. \tag{4.9}$$

It should be noted that the reflection and transmission coefficients are complex valued in general, i.e., the waves are attenuated and phase shifted. Figure 4.2 depicts the coefficients at the boundary between air ($\delta_1 = 1$) and a brick wall ($\delta_2 = 4.44$ [19]). It is emphasized that the TE and TM coefficients are sufficient to describe the reflection and transmission of an arbitrary polarized wave, because any polarization state can be decomposed into a TE and a TM wave. For the purpose of notational convenience, linearly polarized waves are considered in the following.

[1] This is a good approximation for most materials that have a significant impact onto the RF wave propagation [19].

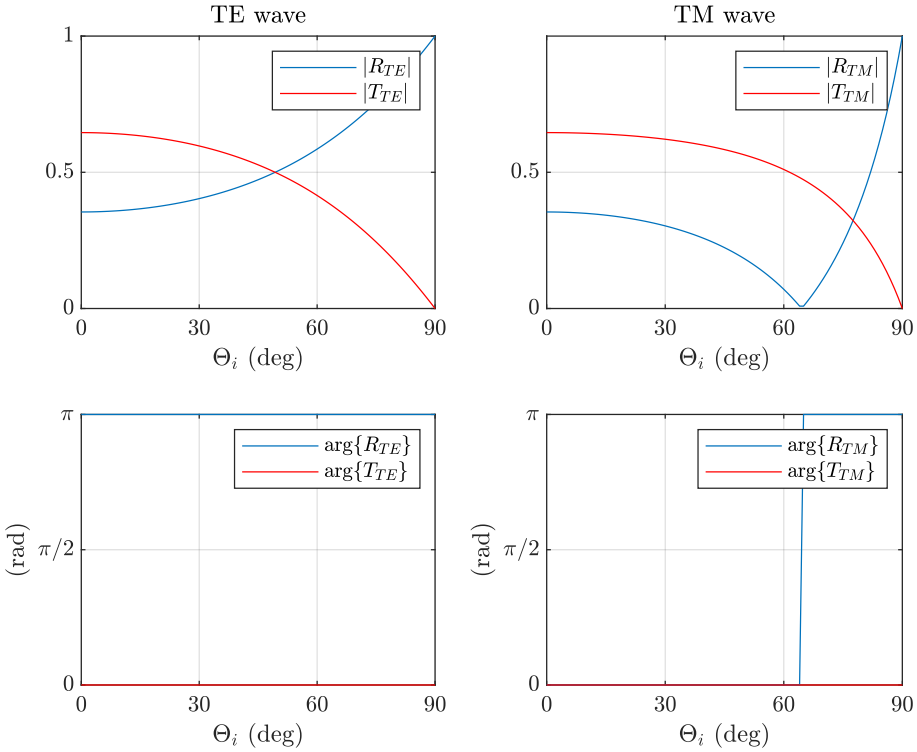

Figure 4.2: Reflection and Transmission Coefficients for $\delta_1 = 1$ and $\delta_2 = 4.44$.

The n^{th} ray arriving at the receiver after M reflections can now be described by[2]

$$\begin{aligned} p_{rx,n}(t,\tau_n) &= \left(\prod_{m=1}^{M} R_{n,m}\right) \tilde{\alpha}_n \exp\{-j2\pi f_c(t+\tau_n)\} \\ &= R_n\, \tilde{\alpha}_n \exp\{-j2\pi f_c(t+\tau_n)\}\,, \end{aligned} \tag{4.10}$$

where $R_{n,m}$ is the reflection coefficient corresponding to the polarization of the wave with respect to the reflecting object, and $\tilde{\alpha}_n$ and τ_n are the free space path loss and delay, introduced by the distance between the virtual transmitter and the receiver. For the LOS path, where no reflection occurs, the reflection coefficient is set to $R_n = 1$. The total received signal is the superposition of N rays

$$p_{rx}(t) = \sum_{n=1}^{N} R_n\, \tilde{\alpha}_n \exp\{-j2\pi f_c(t+\tau_n)\}\,, \tag{4.11}$$

and the received signal strength (RSS) is defined as the squared absolute amplitude of the received signal

[2]This model does not account for obstacles on any path between the transmitter and the receiver, which is valid for the measurement setup in Chapter 5.

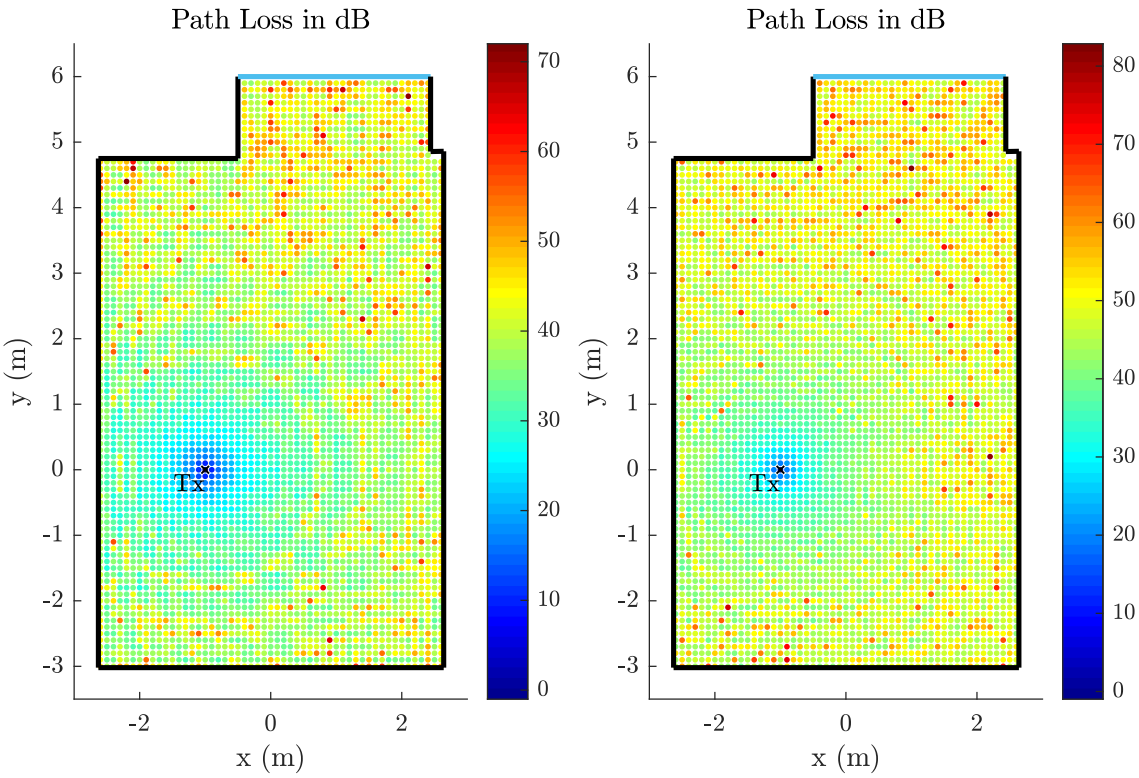

(a) $f_c = 860\,\text{MHz}$ **(b)** $f_c = 2.45\,\text{GHz}$

Figure 4.3: Simulated path loss in a laboratory room. Black lines correspond to plaster board and brick walls. The blue line symbolizes a window. Transmitter and receiver height is 1.45 m.

$$\text{RSS} = \left| \sum_{n=1}^{N} R_n \, \tilde{\alpha}_n \exp\{ -j2\pi f_c(\tau_n) \} \right|^2 = \left| \sum_{n=1}^{N} \alpha_n \right|^2 , \tag{4.12}$$

where the reflection coefficients, free space path losses, and phase shifts, introduced by each path, are absorbed into a single complex coefficient α_n. Figure 4.3 shows the simulated path loss, which is the relation of the transmit signal strength[3] (TSS) to the RSS. Paths with up to two reflections (second order reflection paths) are considered. For higher order reflection paths the attenuation is considered to be too high for a significant contribution to the RSS. The simulated environment is a laboratory room, where the measurements discussed in Chapter 5 were performed. It is apparent that the RSS does not decrease monotonically with an increasing distance to the transmitter. Due to constructive and destructive superposition of the waves from different paths, the RSS is subject to interference patterns. This phenomenon is known as *small-scale fading*. Most prominent are the circular patterns around the transmitter. This is explained by the interference of the LOS component and a strong ground-reflection component. Especially in Figure 4.3a, also radial patterns, originating from the interference with a strong wall-reflection component, can be seen clearly. Comparing Figure 4.3a and 4.3b, it is evident that the periodicity

[3]The transmit signal strength is defined as the squared amplitude of the transmit signal, i.e., $\text{TSS} = |a|^2$, with a from (4.1).

of the patterns varies with the frequency due to different wavelengths. The variation of the RSS, introduced by small-scale fading, poses two main problems on the localization of RFID tags: (i) Passive tags harvest their operating energy from the transmitted CW carrier. In a deep fading hole the RSS might be too low to operate the tag. (ii) If the energy is just sufficient for operation, the signal-to-noise ratio (SNR) might be very low, which affects the ranging accuracy.

4.1.2 Backscatter Channel

The channel from the transmitter to the receiver can now be described in the form of a *tapped delay line* (TDL) model

$$h(\tau) = \sum_{n=1}^{N} R_n \, \tilde{\alpha}_n \exp\{ -j2\pi\tau_n \} \, \delta(\tau - \tau_n) = \sum_{n=1}^{N} \alpha_n \, \delta(\tau - \tau_n) \, . \tag{4.13}$$

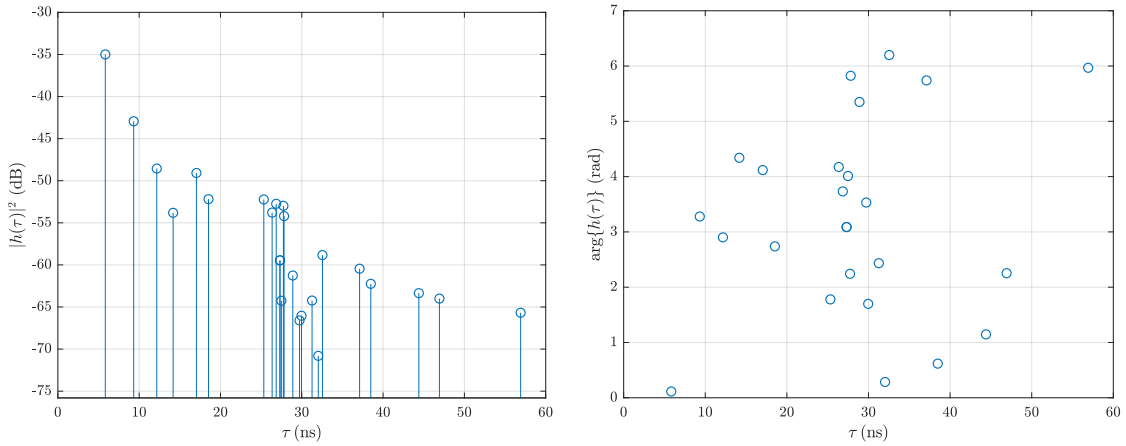

Figure 4.4: Simulated TDL channel at a fixed position in the laboratory room structure at $f_c = 860\,\text{MHz}$.

Figure 4.4 depicts the TDL channel at a fixed location $(x, y, z) = (-1.9, 1.5, 1.45)$ in Figure 4.3a. This point is located in the first strong fading circle around the transmitter. The first and the second tap correspond to the LOS path and the ground-reflection path, respectively. Their relative phase shift is close to π, and therefore, waves traveling along those paths interfere destructively, which leads to a low RSS.
The model (4.13) describes the multipath channel from the transmitter to the receiver at a certain location.[4] But for the ranging of an RFID tag, the behavior of the *backscatter channel*, that is the channel from the transmitter to the tag and from the tag back to the receiver, is of interest (see Figure 3.1). For that matter, let $h_{dl}(\tau)$ denote the channel from the transmitter to the tag (downlink) and $h_{ul}(\tau)$ the channel from the tag to the receiver (uplink). The combined backscatter channel is then given by the convolution

[4] All α_n and τ_n are dependent on the locations of the transmitter and the receiver. In order to keep the notation uncluttered, this dependence is not stated explicitly, but should always be beared in mind.

$$h_{bs}(\tau) = h_{dl}(\tau) * h_{ul}(\tau) \,. \tag{4.14}$$

It is emphasized that this model is strictly valid for a single frequency only. The temporal resolution of ToF localization depends on the signal bandwidth, which should be as large as possible. Therefore, a wideband consideration is needed in order describe the channel for the entire frequency range of the maintained system. One approach is to simulate the channel model (4.13) for multiple frequencies within the used band and combine the results according to [22].

4.1.3 Antennas

Up to this point, isotropic transmitters and receivers with constant gain $G_{tx} = G_{rx} = 1$ are assumed. In order to account for the directivity and gain of real antennas, a frequency and angle dependent antenna gain factor is introduced. It is defined as the ratio of the power received by the used antenna from a far-field source in a certain direction, and the power received by a lossless isotropic antenna from the same source

$$G^{(h,v)}(\vartheta, \varphi, f) = \frac{P_{rx}^{(h,v)}(\vartheta, \varphi, f)}{P_{rx,i}(f)} \,, \tag{4.15}$$

where ϑ and φ are the azimuth and elevation angles, respectively. The superscript denotes the polarization, where h is horizontal, and v is vertical to the ϑ-φ-direction. Including the antenna gain factor for the transmitter and the receiver, the TDL channel (4.13) is now[5]

$$g(\tau) = \sum_{n=1}^{N} \sqrt{G_{tx,n}\, G_{rx,n}}\, \alpha_n\, \delta(\tau - \tau_n) \,, \tag{4.16}$$

where $G_{tx,n}$ is the gain of the transmit antenna in the direction of the n^{th} ray leaving the transmitter and $G_{rx,n}$ is the gain of the receive antenna in the direction of the n^{th} ray arriving at the receiver.
Figure 4.5 shows the simulated path loss including the transmit antenna gain G_{tx} of a Huber&Suhner SPA-8090/78/8/0/V antenna, which was used in the measurements described in Chapter 5. The receive antenna gain is set to $G_{rx} = 1$, i.e., the tag is assumed to be isotropic.

[5] Both G_n and α_n depend on the frequency, direction, and polarization, which is not stated explicitly, to keep the notation simple.

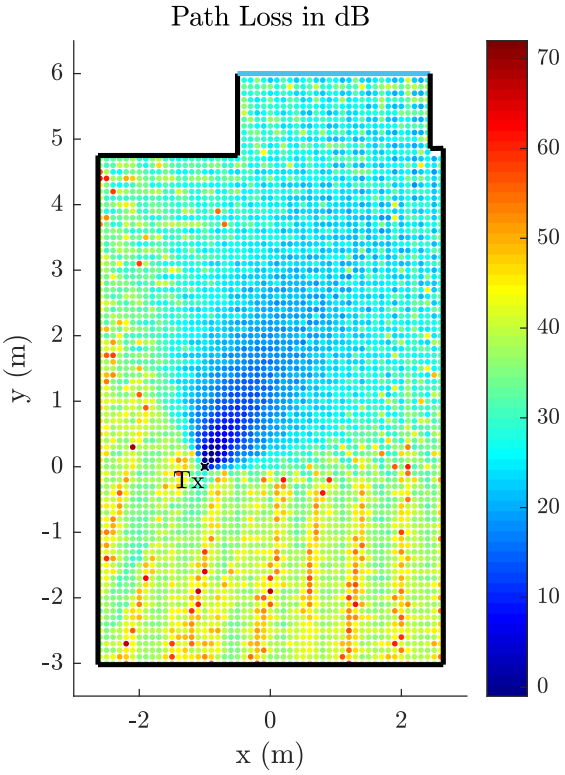

Figure 4.5: Simulated path loss at $f_c = 860\,\text{MHz}$, including the transmit antenna gain G_{tx}. Transmitter and receiver height is 1.45 m.

4.2 Statistical Model Extension

The ray tracing model in the previous section accounts for multipath components due to reflections at flat surfaces. However, a wireless channel is also subject to scattering effects, i.e., there are additional multipath components due to scattering at small[6] objects and rough surfaces. As the deterministic simulation of such effects is intractable, a stochastic description is required. The *Saleh-Valenzuela model*, proposed in [17], is a simple formulation that can easily be combined with the results of ray tracing. Several measurements, for example [17] and [23], show that multipath components arrive in clusters. Each cluster starts with a strong component and decays exponentially afterwards. The Saleh-Valenzuela model gives a statistical description of the amplitudes and arrival times of both the components within a cluster and the clusters themselves. The arrival time T_n of the n^{th} cluster and the arrival time $t_{n,k}$ of the k^{th} component within the n^{th} cluster are modeled by independent exponential pdf's conditioned on the previous value

$$f_{\mathsf{T}_n|\mathsf{T}_{n-1}}(T_n|T_{n-1}) = \Lambda \exp\big\{ -\Lambda\,(T_n - T_{n-1})\big\}\,, \tag{4.17}$$

and

$$f_{\mathsf{t}_{n,k}|\mathsf{t}_{n,k-1}}(t_{n,k}|t_{n,k-1}) = \lambda \exp\big\{ -\lambda\,(t_{n,k} - t_{n,k-1})\big\}\,, \tag{4.18}$$

[6] Comparable to the size of the wavelength.

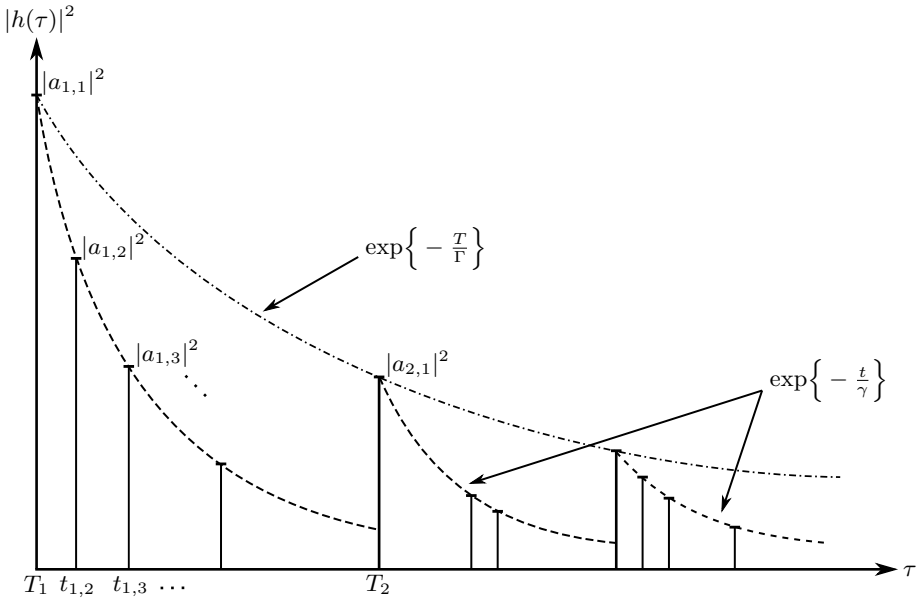

Figure 4.6: Schematic representation of the Saleh-Valenzuela model.

where Λ and λ are constant arrival rate factors and $k, n \in \mathbb{N}_+$. The squared absolute value of the k^{th} component within the n^{th} cluster is modeled to be

$$|\alpha_{n,k}|^2 = \overline{|\alpha_{1,1}|^2} \exp\left\{-\frac{T_n}{\Gamma}\right\} \exp\left\{-\frac{t_{n,k}}{\gamma}\right\}, \tag{4.19}$$

where $\overline{|\alpha_{1,1}|^2}$ is the mean of the squared absolute value of the first component in the first cluster and $|\alpha_{1,1}|^2$ follows an exponential distribution. The constant factors Γ and γ are the decay parameters. A schematic representation of the Saleh-Valenzuela model is shown in Figure 4.6.
The ray tracing and the Saleh-Valenzuela model can now be combined by considering the multipath components calculated by the ray tracer as the first components of the clusters. Thus, the cluster arrival times (4.17) can be ignored and (4.19) is replaced by

$$|\alpha_{n,k}|^2 = |\alpha_n|^2 \exp\left\{-\frac{t_{n,k}}{\gamma}\right\}, \tag{4.20}$$

where the α_n's are taken from (4.13). The TDL channel obtained by the combined model is now

$$h(\tau) = \sum_{n=1}^{N} \sum_{k=1}^{\infty} \alpha_{n,k}\, \delta(\tau - \tau_{n,k}), \tag{4.21}$$

and the phase information of the complex $\alpha_{n,k}$'s that are not given by the ray tracer is

drawn from a uniform distribution between $-\pi$ and π, as suggested in [17]. Although k extends to infinity, it can be truncated whenever $|\alpha_{n,k}|$ falls below a given threshold. Finally, as in the previous section, the backscatter channel is given by (4.14), with h_{dl} and h_{ul} obtained from (4.21).

In order to gain information about the parameters of a practical RFID system, that influence the behavior of the localization methods, discussed in Chapter 3, the measurement setup, described in Chapter 5, is emulated by the ray tracing model. The transmission of the DSSS signal over the synthetic channel is simulated and the range estimators are applied to both, the simulated and the measured receive signals. The results are compared in Chapter 6.

5 Measurements

During the "REFlex"-project[1] a system was developed that implements the method described in Section 3.1. This system was used to perform a measurement campaign in a laboratory room at the TU Wien.[2] The results of these measurements are used to evaluate the localization algorithms discussed in Chapter 3. Section 5.1 provides a brief description of the testbed architecture and Section 5.2 explains the measurement setup.

5.1 Testbed Architecture

5.1.1 RFID Tag

The EPC Class-1 Gen-2 UHF RFID standard operates in the 860–960 MHz frequency range. With the aid of the method described in Section 3.1, where a low power DSSS signal is superimposed onto the RF carrier during the tag to reader communication, a bandwidth large enough for high accuracy ToF estimation is reached. However, the application of this method in the UHF band comes with two problems: (i) The tag antennas in this range have a frequency selective gain and group delay within the used bandwidth. (ii) The spectral mask requirements limit the power of the DSSS signal, which implies a low SNR. In order to solve these problems, a dual-frequency tag was developed by NXP, which extends a UCODE 7 tag with a second port, connected to a separate antenna. This way, the EPC compliant communication is performed in the UHF band and the DSSS transmission in both the UHF and the 2.45 GHz ISM band. The spectral mask requirements in the 2.45 GHz ISM band allow for a higher power density, resulting in a higher SNR. Furthermore, the antenna for the 2.45 GHz ISM band can be designed to have a more constant frequency response over the entire range.

5.1.2 RFID Reader

The RFID readers are USRP-2922 software defined radio (SDR) platforms from National Instruments with a slightly modified SBX daughter board. In [24], an RFID reader was

[1] "RFID Real-Time Localization for Flexible Production Environments" (REFlex) was a research project founded by the Austrian Research Promotion Agency (FFG); Project number 845630.

[2] The author of this work was not part of the "REFlex"-project, but supported the measurement campaign.

implemented, that is capable of performing EPC Gen-2 compliant communication and the cyclic alignment procedure described in Section 3.1. Due to the large bandwidth and high resolution, needed for ToF localization, the data rates are too high for transmission over an Ethernet connection using the standard SDR framework. Furthermore, stringent timing requirements have to be fulfilled for the EPC communication with the tag. Thus, the cyclic alignment and averaging is directly done in the user accessible FPGA of the SDR, which significantly reduces the required data rates. In order to perform coherent MIMO measurements, synchronization of the USRPs over a dedicated "MIMO link" and a modified local oscillator (LO) distribution were developed in [25].
Each USRP has an RF input and an RF output, allowing for bistatic measurements. The USRPs are connected to a PC for controlling and data transfer via Ethernet link. The sampling frequency is 100 MHz and the DACs and ADCs have a bit depth of 16 bit and 14 bit, respectively.

5.2 Measurement Setup

Figure 5.1 depicts the block diagram of the MIMO setup. The measurements were performed with four USRPs, each connected to one transmit and one receive antenna. USRP 1 acts as master, and USRP 2–4 as slaves. The master is responsible for the EPC communication and the transmission of the DSSS signal in the UHF band. The slaves perform the transmission of the DSSS signal at 2.45 GHz.
USRP 1 is connected to a 10 MHz clock reference. Synchronization of all USRPs in the 100 MHz domain is carried out by the MIMO extension. The master transmits a synchronization signal, which is distributed to all slaves via the MIMO splitter.
Due to the modification of the SBX daughter board, the inputs and outputs of the transmit and receive LOs are accessible from the outside. USRP 1 is the only one operating in the UHF band, thus, only its own transmit and receive LOs have to be synchronized. Therefore, the receive LO output is fed into the receive and transmit LO inputs via a two-way zero degree power splitter. USRP 2–4 have to perform coherent measurements at 2.45 GHz. The LO output of USRP 2 is therefore fed into all LO inputs via power splitters. To compensate for the losses of the cables and power splitters, a ZX60-83LN-S+ amplifier from Mini-Circuits is used.
The antennas for the UHF and the ISM bands are Huber&Suhner SPA-8090/78/8/0/V and SPA-2400/75/9/0/V antennas, respectively. The signal for the EPC communication was transmitted with an EIRP of 35.05 dBm, which is the highest admissible transmit power for RFID systems in the 860–960 MHz band [26]. The power amplifier ZHL-30W-252+ from Mini Circuits is placed in front of the UHF transmit antenna, because the USRP is not able to provide such a high output power. In order to fulfill the spectral mask requirements of the EPC standard, the DSSS signal power has to be 40.9 dB lower than the signal power for the EPC communication, resulting in an EIRP of −5.85 dBm in the UHF band. With an EIRP of 10 dBm, the maximum allowed power in the 2.45 GHz ISM band is significantly higher. Here, the DSSS signal was transmitted with an EIRP of 8 dBm. The bandwidth was limited to about 83 MHz by the baseband filters of the USRPs [27].

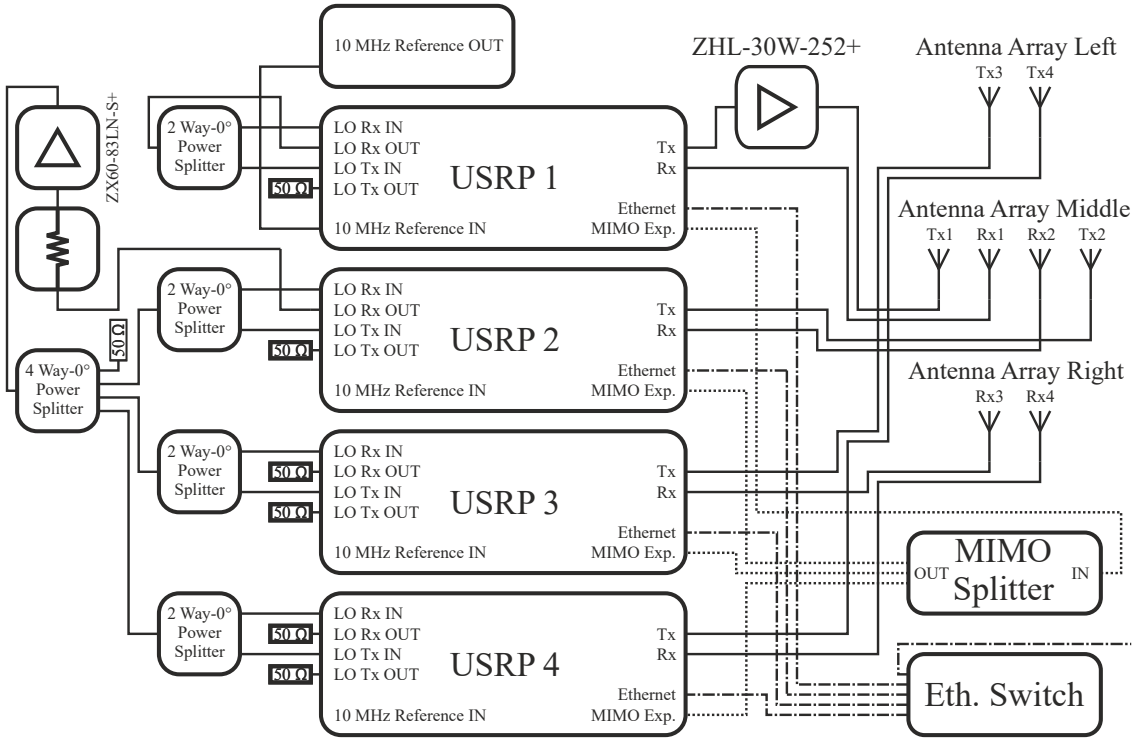

Figure 5.1: Block diagram of the measurement setup. [28]

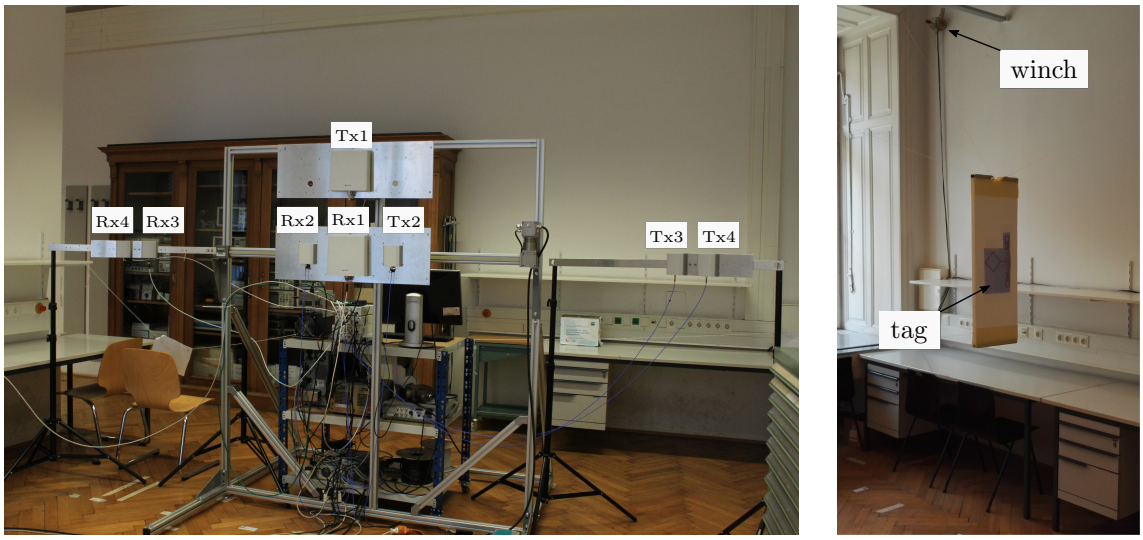

(a) **(b)**

Figure 5.2: **(a)** Picture of the measurement setup. **(b)** Picture of the tag on the Rohacell block, placed in the center of the room by the positioning system.

In order to accurately place the tag in the room, an automatic positioning system was installed. Four winches, mounted at the top corners of the room are connected to a

Rohacell[3] block, to which the tag was sticked (see Figure 5.2b). The tag was placed in 0.1 m steps in an area of 3.6 m × 3.8 m. The hight of the tag and the 2.45 GHz ISM antenna positions was 1.45 m and the heights of UHF transmit and receive antenna were 1.85 m and 1.45 m, respectively. Figure 5.2a shows a picture of the measurement setup in a laboratory room at the TU Wien.

[3]Rohacell is the trade name of Polymethacrylimid. It was chosen because of its dielectric properties, which are close to those of air, in order to minimize the influence on the measurement.

6 Results

In order to evaluate the algorithms presented in Chapter 3, they are applied to simulated data, using the channel obtained by the ray tracing method described in Chapter 4, and to measured data obtained by the measurement campaign described in Chapter 5.

The DSSS sequence is a maximum length sequence with a chip rate of 50 Mchips/s and a length of 1022 samples. The receive signal is averaged over 100 recordings per tag position, to increase the SNR. The sample covariance estimator (3.46) for a fixed tag position includes the receive signal for all adjacent tag positions within a distance of 0.1 m.
For the evaluation of the ranging accuracy, the range estimation error is defined as

$$\varepsilon_d = d - \hat{d}\,, \tag{6.1}$$

where d and $\hat{d}$ are the true and estimated distances, respectively.

6.1 Tag Impulse Response Compensation

It is mentioned in Section 3.2 that the channel model (3.6) assumes an ideal delta impulse response $\Delta h_{tag}(t)$ of the tag, which is not true in practice. In order to account for the tags' delta impulse response, the following procedure includes $\Delta h_{tag}(t)$ into the transmit signal for the estimators in Chapter 3. Considering the receive signal (3.8) for a known tag position, and including $\Delta h_{tag}(t)$, it can be written as

$$r_{kk'}(t) = \left[\alpha_{kk'} s(t-\tau_{kk'}) \exp\{-j(2\pi f_c \tau_{kk'})\}\right] * \Delta h_{tag}(t) + \left(s * \nu_{kk'} * \Delta h_{tag}\right)(t) + w(t)\,. \tag{6.2}$$

The LOS attenuation $\alpha_{kk'}$ contains the free space attenuation, which is known for a known delay $\tau_{kk'}$, and a random phase shift ϕ. The LOS phase shift $\exp\{-j(2\pi f_c \tau_{kk'})\}$ is also known for a known $\tau_{kk'}$. Multiplying (6.2) by $\frac{1}{|\alpha_{kk'}|} \exp\{j(2\pi f_c \tau_{kk'})\}$ and shifting it by $\tau_{kk'}$, the corrected receive signal is

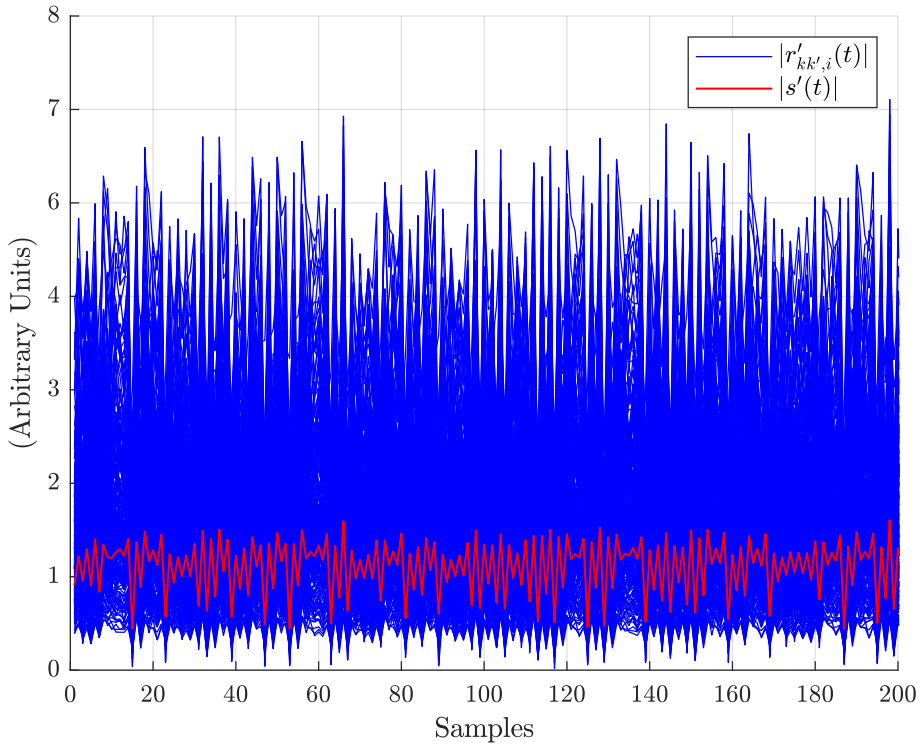

Figure 6.1: 200 Samples of the averaged receive signal.

$$r'_{kk'}(t) = \big(s * \Delta h_{tag}\big)(t)\exp\{j\phi\} + \frac{1}{|\alpha_{kk'}|}\exp\{j(2\pi f_c \tau_{kk'})\}\left[\big(s * \nu_{kk'} * \Delta h_{tag}\big)(t+\tau_{kk'}) + w(t+\tau_{kk'})\right]. \tag{6.3}$$

The multipath $\nu_{kk'}(t)$ and $w(t)$ are assumed to be zero mean Gaussian processes, and the phase ϕ is assumed to be uniformly distributed between $-\pi$ and π. This implies that the average over a large number of tag positions cancels out the phase term and the contribution of the multipath and the noise

$$s'(t) = \big(s * \Delta h_{tag}\big)(t) \approx \sum_{i=1}^{N} r'_{kk',i}(t)\,, \tag{6.4}$$

where i denotes the index of the tag position.

Figure 6.1 shows the new transmit signal $s'(t)$ and the corrected receive signals $r'_{kk',i}(t)$ for $N = 200$ tag positions. If not stated otherwise, the signal $s'(t)$ is used for the evaluation of the measurement data in the following sections. The tag response does not have to be considered for the simulated data, because the channel model already assumes an ideal tag response.

6.2 Dual-Frequency Tag

The following compares the measurements in the UHF band to those in the 2.45 GHz ISM band. As merely Tx1/Rx1 (see Figure 5.2a) perform measurements in the UHF band, the only fair comparison is to Tx2/Rx2, because they are also placed close to the center of the room, which leads to about the same spatial coverage.

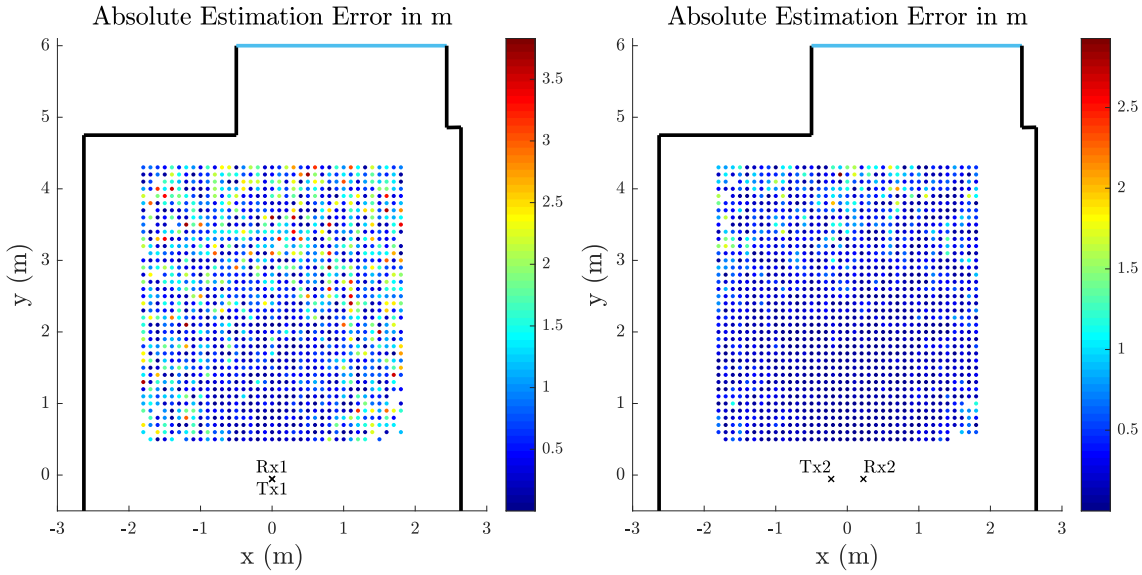

(a) UHF **(b)** 2.45 GHz ISM

Figure 6.2: Absolute range estimation error of the matched filter estimator for the UHF and the 2.45 GHz ISM band. Visualization is truncated at 4 m, which is identified by missing points. It is pointed out to the reader, that **(a)** and **(b)** have different scales.

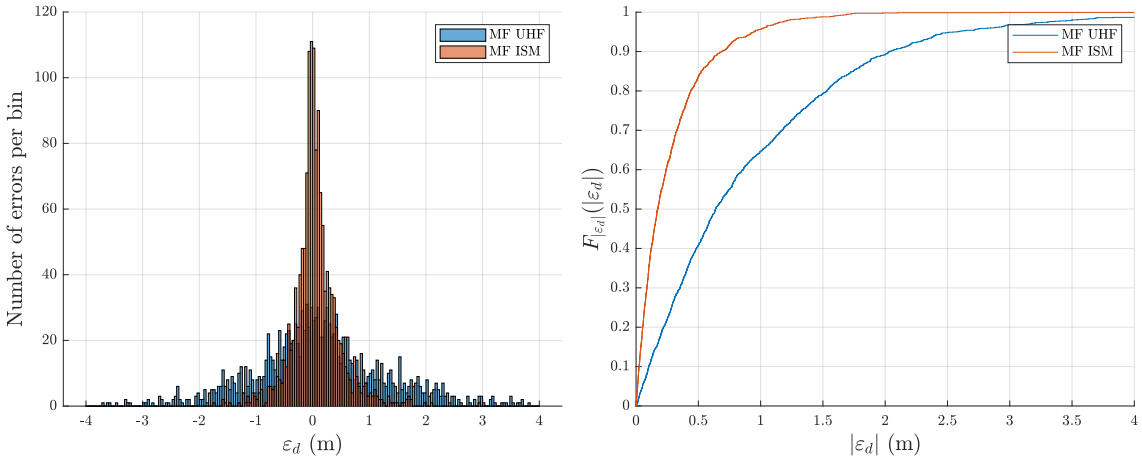

(a) **(b)**

Figure 6.3: Statistical evaluation of the range estimation error for the matched filter estimator in the UHF and the 2.45 GHz ISM band.

Figure 6.2 depicts the absolute value of the estimation error obtained by the matched filter (MF) estimator (3.17) for all tag positions in the room. The visualization for the UHF band shows that the error is smaller than 0.5 m in the near vicinity of the antennas, but varies rapidly outside this area. For the measurements in the 2.45 GHz ISM band, the area of stable range estimation is significantly larger.
Figure 6.3 provides a statistical evaluation of the estimation error. It is seen in Figure 6.3a that the error for both, the UHF and the 2.45 GHz ISM band, is, without consideration of outliers, unbiased. However, the distribution in the 2.45 GHz ISM band is clearly narrower. Figure 6.3b shows the cumulative distribution function (cdf) of the absolute estimation error, denoted by $F_{|\varepsilon_d|}(|\varepsilon_d|)$. The error is less than 0.5 m for 84 % of all positions in the 2.45 GHz ISM band and for 41 % in the UHF band.
The performance difference between the two bands can be explained mainly by the following reasons, shown in [29]: (i) The tag antenna for the 2.45 GHz ISM band is designed to be wideband. (ii) The tag response $\Delta h_{tag}(t)$ in the UHF regime strongly depends on the power of the CW signal that provides the tag with energy. Consequently, the tag response depends on the position of the tag. This is not the case in the 2.45 GHz ISM band. (iii) Due to the smaller relative bandwidth in the 2.45 GHz ISM band, the tag has a more constant frequency response and group delay within the bandwidth of the DSSS signal in the 2.45 GHz ISM band than in the UHF band.

6.3 Matched Filter and Maximum Likelihood Estimation

This section compares the MF estimator to the maximum likelihood estimator in the 2.45 GHz ISM band. The ML estimator uses Tx3/Tx4 as transmit array, and Rx3/Rx4 as receive array. In order to obtain a fair comparison, the mean of the MF estimator applied to every Tx/Rx combination of those arrays is calculated. The transmit and receive antennas are oriented such, that the center of the measurement area is located in the main lobe of the antenna patterns (see Figure 4.5).
It is seen in Figure 6.4, that the estimation error of the MF estimator is mostly less than 0.4 m for $y < 2.5$ m and gets significantly larger for larger distances. The variation of the error for the ML estimator is about the same in the entire measurement area. This can be explained by the fact that the power difference between the LOS component and the multipath components is lower in the back of the room and the ML estimator accounts for the contribution of the multipath, while the MF estimator does not.
A statistical evaluation of the estimation error is provided by Figure 6.5. The estimation error is, again, without consideration of outliers, unbiased. Outliers are positive because they are introduced by strong multipath components, which always arrive after the LOS component at the receiver.
The estimation error of the ML estimator is less than 0.2 m for 97.5 % of all tag positions, while the MF estimator achieves this result in 52.8 %.

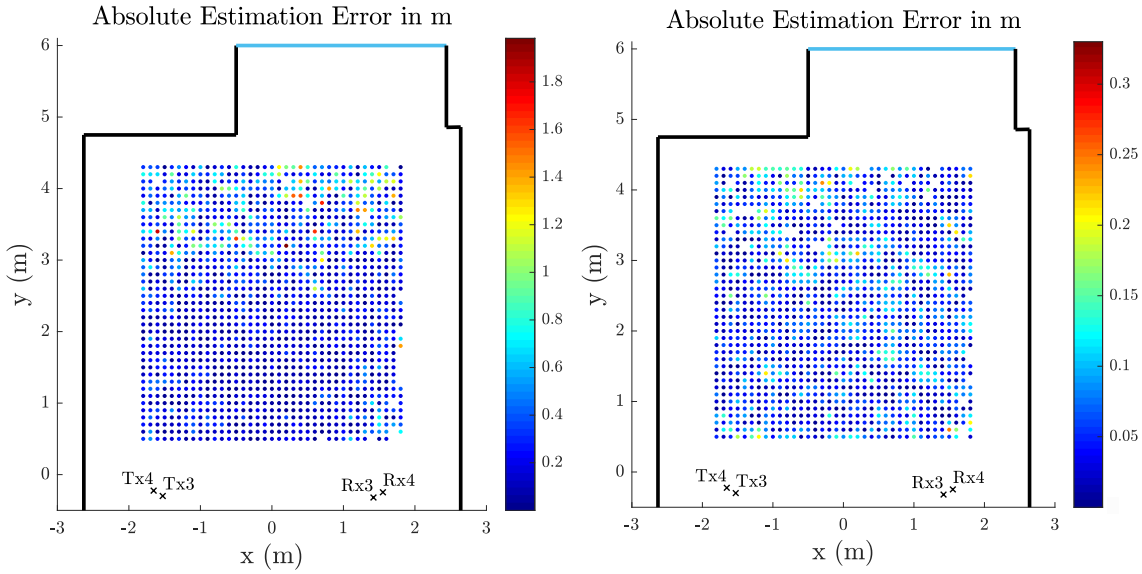

(a) MF **(b)** ML

Figure 6.4: Absolute range estimation error of the MF and ML estimators in the 2.45 GHz ISM band. Visualization is truncated at 2 m, which is identified by missing points. It is pointed out to the reader, that **(a)** and **(b)** have different scales.

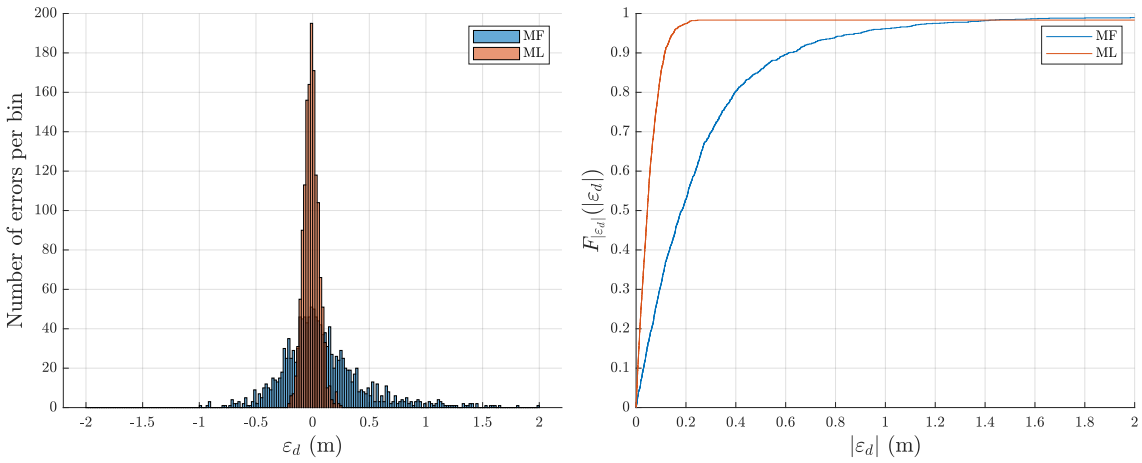

(a) **(b)**

Figure 6.5: Statistical evaluation of the range estimation error for the MF and ML estimators in the the 2.45 GHz ISM band.

6.4 Channel Simulation

In order to evaluate the ranging with respect to the channel model obtained by the ray tracer, described in Chapter 4, the MF and ML estimators are applied to a simulated transmission of the DSSS signal over the synthetic channel. The results are compared to those for the measured data, discussed in Section 6.3.

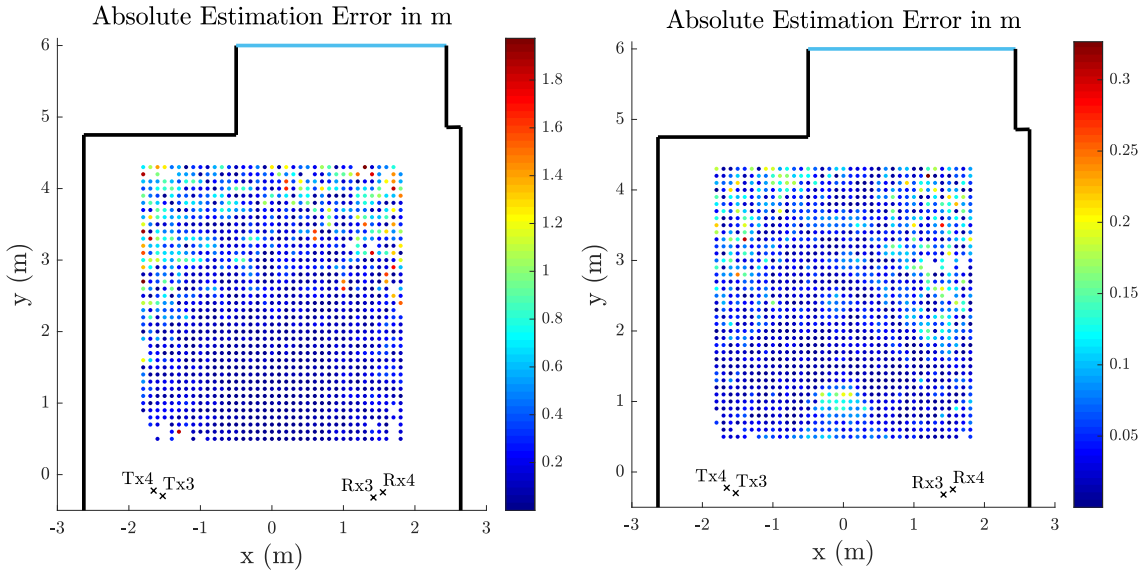

(a) MF **(b)** ML

Figure 6.6: Absolute range estimation error of the MF and ML estimators for the simulated channel in the 2.45 GHz ISM band. Visualization is truncated at 2 m, which is identified by missing points. It is pointed out to the reader, that **(a)** and **(b)** have different scales.

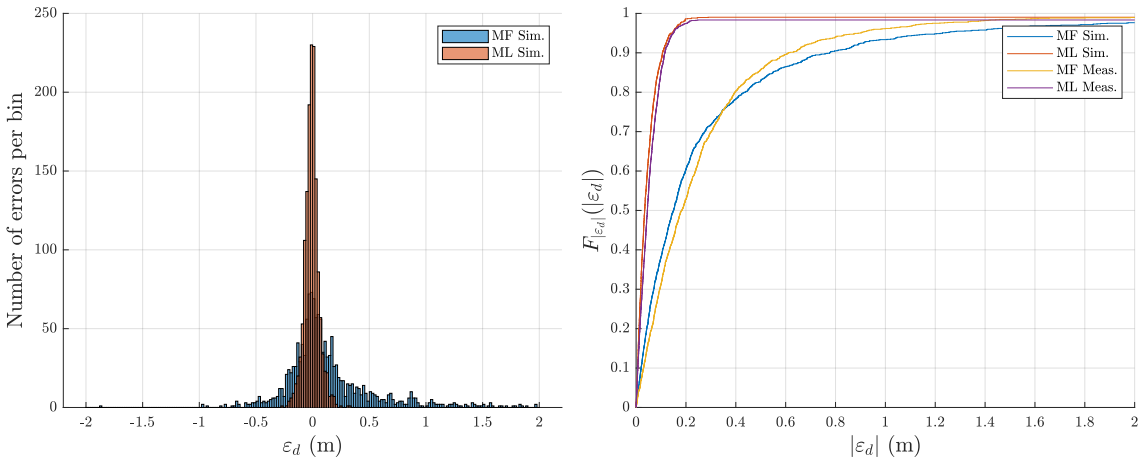

(a) **(b)**

Figure 6.7: Statistical evaluation of the range estimation error of the MF and ML estimators for the simulated channel in the the 2.45 GHz ISM band.

Comparing Figure 6.6 to Figure 6.4, it is seen that the spatial distribution of the ranging error is similar for the simulated and the measured data. Again, the estimation error of the MF estimator is mostly less than 0.4 m for $y < 2.5$ m and gets significantly larger for larger distances. The error of the ML estimator is more constant over the entire area, with a little more outliers in the back of the room.
The statistical evaluation in Figure 6.7 supports this similarity. It is evident, that the cdf of the ML estimation error is almost identical to the one obtained for the measurement

data. Also the cdfs for the MF estimator show very good agreement, with a maximal difference of about 6 %.
These observations draw two important conclusions: (i) The channel model obtained by the ray tracer provides a good approximation of the true channel. (ii) The incorporation of the tag response $\Delta h_{tag}(t)$ into the transmit signal, described in Section 6.1, is valid. This is implied by the fact that the simulated channel model assumes an ideal tag response.

6.5 Tag Impulse Response

For a statement about the impact of the tag response $\Delta h_{tag}(t)$ onto the estimation accuracy, the MF and the ML estimators are applied to the measurement data using the original transmit signal instead of $s'(t)$.
Figure 6.8 and 6.9 show that this impact is significant. The estimators are biased, without consideration of outliers, by 0.5 m and 0.8 m, respectively. In the ML case, outliers appear more frequently than in Section 6.3. However, ignoring them, the width of the distributions for both estimators are not notably wider than in Section 6.3. Figure 6.9b shows the original cdfs and the cdfs corrected for the bias of the estimation error.
It is concluded, that knowledge about the tags' impulse response is crucial. In environments where all tags have the same response, this information can be determined in advance, e.g., by the procedure in Section 6.1. Section 6.4 shows that this leads to results similar to the simulated channel model, which assumes an ideal tag response. However, in environments including different tags from different vendors, the impulse response of the tags might differ significantly and, therefore, such a procedure cannot be applied.

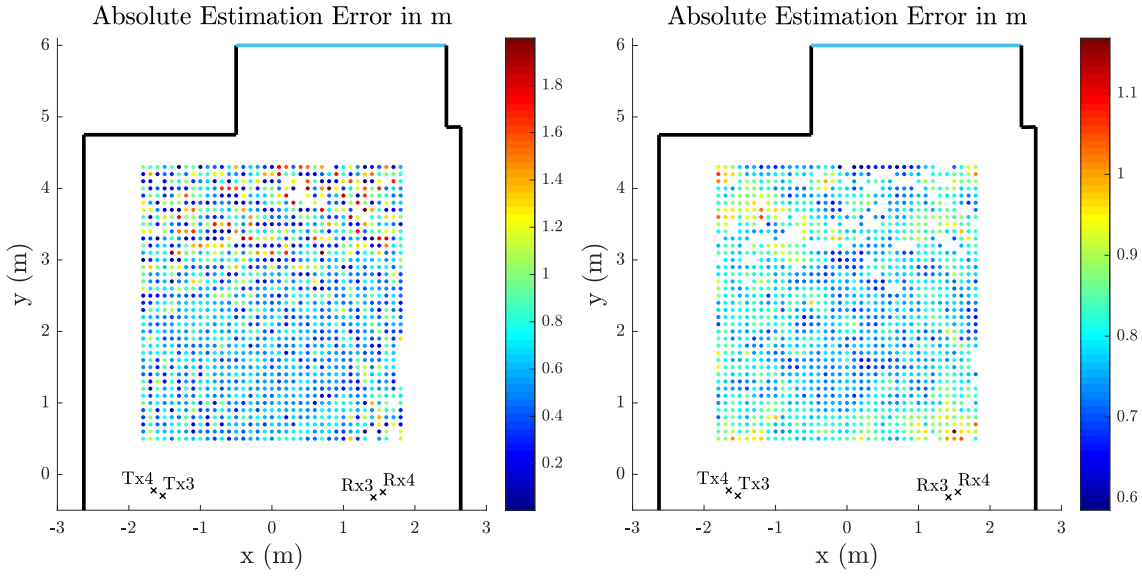

(a) MF **(b)** ML

Figure 6.8: Absolute range estimation error of the MF and ML estimators in the 2.45 GHz ISM band, without consideration of the tag response. Visualization is truncated at 2 m, which is identified by missing points. It is pointed out to the reader, that **(a)** and **(b)** have different scales.

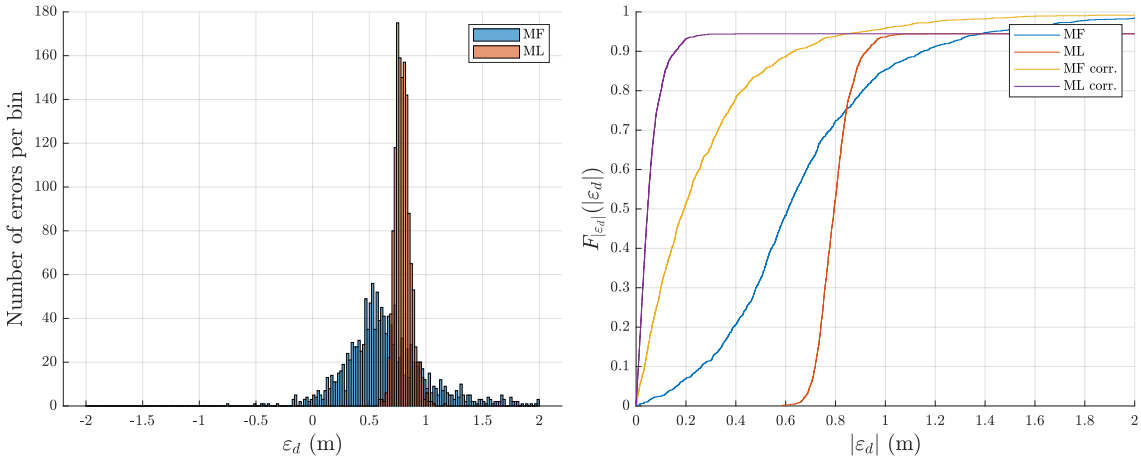

(a) **(b)**

Figure 6.9: Statistical evaluation of the range estimation error for the MF and ML estimators in the the 2.45 GHz ISM band, without consideration of the tag response.

7 Conclusion & Outlook

The focus of this thesis was to evaluate backscatter based RFID localization methods, which use a superimposed, low power wideband signal for time of flight range estimation. To this end, two estimators, based on different channel models, were applied to (i) the results of a comprehensive measurement campaign and (ii) synthetic data obtained from a simulated channel model.

A three dimensional ray tracer was implemented in order to emulate the measurement setup. As this deterministic method only considers the specular components of a multipath channel, it was extended by a statistical model, which, in addition, accounts for diffuse components. With the aim of a valid model for the entire frequency range of the wideband signal, the channel was simulated at multiple frequencies within the utilized bandwidth, and combined into a frequency dependent model.

The measurements were performed under the use of an especially designed, EPC compatible RFID tag, which is capable of backscattering in two different frequency regimes, at 860–960 MHz in the UHF band and in the 2.45 GHz ISM band.

It has been shown that the range estimation results in the 2.45 GHz ISM band are superior to those in the UHF band. This is explained by the wideband antenna design, the power independent tag impulse response, and the more constant frequency response of the tag due to the smaller relative bandwidth in the 2.45 GHz ISM band. Further, the maximum likelihood estimator achieves significantly better results than the matched filter estimator. This is argued by the fact that the first accounts for the multipath contribution and uses the information of multiple antennas, while the latter does not make use of this knowledge.

A comparison of the measured and simulated data shows almost identical results, if the tag impulse response is considered in the range estimation. This observation has two important implications: Primarily, the channel model obtained by the ray tracer is a good approximation of the true channel. Furthermore, knowledge of the tags' impulse response is crucial for accurate range estimation.

The integration of the tag impulse response into the channel simulator is one major subject for a future extension of this work. Additionally, it should be investigated if the channel simulation is still valid for different environments.

References

[1] J. Landt. The history of RFID. *IEEE Potentials*, 24:8–11, 2005.

[2] S. Ahson and I. Mohammed. *RFID Handbook: Applications, Technology, Security, and Privacy*. CRC Press, Boca Raton, FL, 2008.

[3] D. M. Dobkin. *The RF in RFID: UHF RFID in Practice*. Newnes, Burlington, MA, 2008.

[4] K. Finkenzeller. *RFID Handbook: Fundamentals and Applications in Contactless Smart Cards, Radio Frequency Identification and Near-Field Communication*. John Wiley & Sons, Chichester, West Sussex, 3 edition, 2010.

[5] H. Stockman. Communication by means of reflected power. *Proc. IRE*, 36:1196–1204, October 1948.

[6] L. Ladav and E. Mozeson. *Radar Signals*. John Wiley & Sons, Hoboken, NJ, 2004.

[7] M. A. Richards. *Fundamentals of radar signal processing*. McGraw-Hill, New York, NY, 2005.

[8] H. Arthaber, T. Faseth, and F. Galler. Spread-spectrum based ranging of passive UHF EPC RFID tags. *IEEE Communications Letters*, 19(10):1734–1737, 2015.

[9] GS1 EPCglobal. EPC compliant generation-2 UHF RFID device conformance requirements. *EPCglobal Inc., November*, 2013.

[10] B. C. Levy. *Principles of Signal Detection and Parameter Estimation*. Springer, New York, NY, 2008.

[11] S. M. Kay. *Fundamentals of Statistical Signal Processing: Estimation Theory*. Prentice-Hall, Englewood Cliffs, NJ, 1993.

[12] C. M. Bishop. *Pattern Recognition and Machine Learning*. Springer, New York, NY, 2006.

[13] C. P. Robert and G. Casella. *Monte Carlo Statistical Methods*. Springer, Berlin, Heidelberg, 2 edition, 2004.

[14] GS1 EPCglobal. EPC radio-frequency identity protocols generation-2 UHF RFID; specification for RFID air interface protocol for communications at 860 MHz–960 MHz. *EPCglobal Inc., October*, 2015.

[15] A. F. Molisch. Ultra-wide-band propagation channels. *Proceedings of the IEEE*, 97(2):353–371, 2009.

[16] S. Hinteregger, J. Kulmer, M. Goller, F. Galler, H. Arthaber, and K. Witrisal. UHF-RFID backscatter channel analysis for accurate wideband ranging. *IEEE International Conference on RFID*, 2017.

[17] A. M. A. Saleh and A. R. Valenzuela. A statistical model for indoor multipath propagation. *IEEE Journal on Selected Areas in Communications*, 5(2):128–137, 1987.

[18] S. Grebien, J. Kulmer, F. Galler, M. Goller, E. Leitinger, H. Arthaber, and K. Witrisal. Range estimation and performance limits for UHF-RFID backscatter channels. *IEEE Journal of Radio Frequency Identification*, 1(1):39–50, 2017.

[19] A. F. Molisch. *Wireless Communications*. John Wiley & Sons, Chichester, West Sussex, 2 edition, 2011.

[20] H. L. Van Trees. *Optimum Array Processing: Part IV of Detection, Estimation, and Modulation Theory*. John Wiley & Sons, New York, NY, 2002.

[21] G. Matz. Recursive MMSE estimation of wireless channels based on training data and structured correlation learning. *IEEE/SP 13th Workshop on Statistical Signal Processing, 2005*, 2005.

[22] H. Sugahara, Y. Watanabe, T. Ono, K. Okanoue, and S. Yarnazaki. Development and experimental evaluations of 'RS-2000'–a propagation simulator for UWB systems. *Proceedings IEEE UWBST 04*, pages 76–80, 2004.

[23] J. Karedal, S. Wyne, P. Almers, F. Tufvesson, and A. F. Molisch. UWB channel measurements in an industrial environment. *IEEE Global Telecommunications Conference, 2004. GLOBECOM '04.*, 6:3511–3516, 2004.

[24] F. Galler, T. Faseth, and H. Arthaber. SDR based EPC UHF RFID reader DS-SS localization testbed. *Wireless and Microwave Technology Conference (WAMICON), 2015 IEEE 16th Annual*, pages 1–4, 2015.

[25] F. Galler, S. Grebien, T. Faseth, K. Witrisal, G. Magerl, and H. Arthaber. Extension of an SDR UHF RFID testbed for MIMO and monostatic time of flight based ranging. *IEEE Journal of Radio Frequency Identification*, 1(1):32–38, March 2017.

[26] EPCglobal, GS1. Regulatory status for using RFID in the EPC Gen 2 band (860 to 960 MHz) of the UHF spectrum. `https://www.gs1.at/fileadmin/user_upload/UHF_Regulations.pdf`, 2014. [Online; accessed July 16, 2019].

[27] F. Galler, T. Faseth, and H. Arthaber. Implementation aspects of an SDR based EPC RFID reader testbed. *2015 International EURASIP Workshop on RFID Technology (EURFID)*, 2015.

[28] F. Galler. *Localization of Passive UHF RFID Tags.* PhD thesis, Technische Universität Wien, 2019. unpublished thesis.

[29] D. Neunteufel. Delta-RCS characterization of RFID tags and implications on localization accuracy. Master's thesis, Technische Universität Wien, Wien, 2018.

Hiermit erkläre ich, dass die vorliegende Arbeit gemäß dem Code of Conduct – Regeln zur Sicherung guter wissenschaftlicher Praxis (in der aktuellen Fassung des jeweiligen Mitteilungsblattes der TU Wien), insbesondere ohne unzulässige Hilfe Dritter und ohne Benutzung anderer als der angegebenen Hilfsmittel, angefertigt wurde. Die aus anderen Quellen direkt oder indirekt übernommenen Daten und Konzepte sind unter Angabe der Quelle gekennzeichnet.
Die Arbeit wurde bisher weder im In– noch im Ausland in gleicher oder in ähnlicher Form in anderen Prüfungsverfahren vorgelegt.

Wien, 14. Juli 2019 *Stefan Hechenberger*